POLITECNICO DI TORINO

Master's Degree in Biomedical Engineering

Politecnico di Torino

Master's Degree Thesis

Photoacoustic Imaging and High-Density Surface Electromyography: A Feasibility Study on Muscle Fatigue Monitoring

Supervisors

Prof. Kristen MEIBURGER

Prof. Alberto BOTTER

Prof. Silvia SEONI

Dr. Marco CARBONARO

Candidate

Matteo GARRIONE

October 2025

Summary

Muscle fatigue, defined as the decline in skeletal muscle force or power during sustained activity, is a complex, multifactorial phenomenon critical to physical performance. While myoelectric manifestations are well studied, simultaneous hemodynamic assessment is emerging. Unlike near-infrared spectroscopy (NIRS), this study employs photoacoustic imaging (PAI), combining laser illumination and ultrasound detection for enhanced depth sensitivity. Simultaneous high-density surface electromyography (HD-sEMG) and multispectral PAI were performed using a Verasonics Vantage 256 system with an Opotek Phocus Mobile SE laser and a 128-element linear ultrasound transducer, acquiring 10 wavelengths per acquisition. HD-sEMG was recorded via a 32-channel electrode matrix over the forearm. Two healthy subjects completed two to four trials of rest and sustained isometric contraction (little finger, right hand, until exhaustion), yielding a preliminary multimodal dataset. HD-sEMG signals were analyzed via root mean square (RMS) mapping at contraction start, middle, and end, and RMS and mean frequency (MNF) slopes in the most active muscle region. PAI data were reconstructed and unmixed into oxygenated hemoglobin over total hemoglobin (HbO_2/HbT) distributions. HD-sEMG enabled localized muscle activation assessment, showing trends consistent with fatigue. PAI provided localized monitoring of muscle oxygenation, although quantitative interpretation was constrained by the linear transducer geometry and the linear spectral unmixing algorithm. Despite these limitations, the results demonstrate the feasibility of simultaneous multimodal acquisition, enabling localized monitoring of muscle activity and preliminary observation of fatigue-related changes. This study lays the groundwork for future investigations aimed at refining multimodal assessment of muscle fatigue.

Acknowledgements

ACKNOWLEDGMENTS

"I would like to express my deepest gratitude to my family for their unconditional love, support, and encouragement throughout my academic journey. Their constant belief in me has been my greatest motivation, and I am truly grateful for their patience, understanding, and unwavering presence in every step of this process."

Matteo Garrione

Table of Contents

List of Tables

List of Figures

Acronyms

US
ultrasound

EMG
electromyographic

sEMG
surface electromyography

HD-sEMG
high-density surface electromyography

MUAP
motor unit action potential

PAI
photoacoustic imaging

PA
photoacoustic

NIRS
near-infrared spectroscopy

ADP
adenosine diphosphate

ATP
adenosine triphosphate

SR

sarcoplasmatic reticulum

MU

motor unit

PCr

phosphocreatine

EDM

extensor digiti minimi

EDC

extensor digitorum communis

MHC

myosin heavy chain

Pi

inorganic phosphate

DOT

diffuse optical tomography

HbO_2

oxygenated hemoglobin

Hb

deoxygenated hemoglobin

HbT

total hemoglobin

CV

conduction velocity

MNF

mean frequency

MDF

median frequency

ARV

average rectified value

RMS

root mean square

ROI

region of interest

DAS

delay-and-sum

PSD

power spectral density

SD

single differential

SNR

signal-to-noise ratio

Chapter 1

Introduction

Muscle fatigue is defined in different ways in literature, depending on the context. In medicine and sports science, it is commonly described as a decline in physical performance, accompanied by an increased actual and/or perceived difficulty of the task [1]. In physiology, it is often defined as a reversible reduction in muscle performance that occurs during intensive activity and recovers with rest [2]. More specifically, exercise physiology describes muscle fatigue as a gradual decline in the maximal force or power that muscles can generate, beginning soon after the onset of sustained activity and worsening over time [3]. It can also be understood as the inability of muscles to maintain the required strength during exercise [1, 4].

The effects of fatigue can vary depending on the nature of the task: while maximal contractions lead to a clear decrease in performance as fatigue sets in, submaximal efforts, more common in daily activities, may not show immediate impairments in task performance and failure to complete a task may not be directly due to fatigue of the primary muscles involved [3]. However, in such cases, fatigue eventually manifests as the inability to sustain the activity at its original intensity, a state often referred to as exhaustion [2].

Muscle fatigue has been extensively studied for over a century due to its critical role in physical performance regulation. It serves as a protective mechanism, preventing excessive strain on the musculoskeletal and metabolic systems by triggering sensations of discomfort and exhaustion. These signals prompt adjustments in exercise intensity and duration, ultimately safeguarding the body from potential damage [1, 5]. The detection and classification of muscle fatigue contributes valuable insights to fields such as human-computer interaction, sports performance, ergonomics, and prosthetics. In sports, for instance, muscle fatigue can increase the risk of injury, as overworked muscles may struggle to maintain proper function, leading to strain or damage. While localized fatigue can be beneficial for muscle growth in specific settings, such as bodybuilding, in occupational health and ergonomics, it poses risks for musculoskeletal disorders. Predicting fatigue in these contexts can

help prevent injuries, particularly in tasks requiring sustained static muscle activity or poor posture. Proactively addressing muscle fatigue is thus essential for reducing injury risks and supporting long-term health and performance [6]. When fatigue accumulates without adequate recovery, it can contribute to conditions like chronic fatigue syndrome and overtraining syndrome. In severe cases, prolonged fatigue may even lead to endocrine imbalances, immune dysfunction, or other health risks, highlighting the importance of recognizing and managing fatigue to prevent both immediate and long-term effects on health and performance [7].

To fully understand muscle fatigue, both structural changes and functional impairments need to be examined. This thesis aims to explore the potential of integrating two advanced imaging and sensing modalities such as photoacoustic imaging (PAI) and high-density surface electromyography (HD-sEMG), to provide a comprehensive assessment of muscle fatigue. By combining these techniques, it is possible to investigate both the vascular and oxygenation dynamics underlying muscle fatigue, as well as the associated neuromuscular activation patterns. This integrated approach has the potential to enhance our understanding of fatigue mechanisms, offering valuable insights for applications in clinical rehabilitation, sports performance optimization, and ergonomics.

The remainder of this thesis is structured as follows: Chapter 2 provides the theoretical background of the study, introducing the fundamental concepts of muscle fatigue and the principles of the non-invasive techniques employed. Chapter 3 describes the experimental setup, acquisition procedures, and data processing methods. Chapter 4 presents the results obtained from PAI and HD-sEMG, followed by their integrated analysis. Finally, Chapter 5 discusses the findings in relation to existing literature, highlighting strengths, limitations, and potential improvements.

Chapter 2

Theoretical background

The following section provides the theoretical background necessary to understand the experimental work presented in this thesis. It begins with an overview of skeletal muscle physiology, with particular attention to excitation–contraction coupling and force generation. The mechanisms underlying muscle fatigue are then discussed, highlighting both peripheral and central contributors as well as their biochemical and neuromuscular correlates. Finally, the section reviews the principles of the imaging and electrophysiological techniques employed in this study, namely US/PA imaging and HD-sEMG.

2.1 Skeletal muscle structure and function

Skeletal muscles play a central role in human movement and force generation, and their properties can be described at different levels of organization, from cellular structure to whole-muscle mechanics. This section provides an overview of the main physiological principles relevant to this thesis, including the cellular and molecular architecture of skeletal muscle, the mechanisms of force generation and regulation, and the metabolic pathways that sustain contraction. Unless otherwise specified, the following information is adapted from [8].

2.1.1 Cellular and molecular structure of skeletal muscles

The effector organ of the somatic nervous system is skeletal muscle. However, in muscle tissue, action potentials have a different effect compared to nervous tissue, as they trigger contractions and force generation. A typical skeletal muscle cell can activate its contractile mechanism within milliseconds of receiving the neural signal and can deactivate it almost as quickly. With some exceptions, skeletal muscles are connected to at least two bones via tendons.

The part of the muscle responsible for force generation is called the body, or the "fleshy" portion of the muscle. The connective tissue forming the tendon is continuous with the layer surrounding the muscle body, known as the epimysium. Another layer of connective tissue, the perimysium, extends within the muscle body, dividing it into numerous bundles called fascicles, which are composed of individual muscle cells. Each fascicle contains hundreds to thousands of muscle cells, known as muscle fibers, each of which extends the entire length of the muscle. The nuclei of muscle fibers are located just beneath the plasma membrane, known as the sarcolemma. Muscle fibers generate contractile force by utilizing energy released from adenosine triphosphate (ATP) hydrolysis. Within the fibers, there are myofibrils, which contain the contractile machinery. Each myofibril consists of a bundle of thick and thin filaments that overlap, primarily composed of the proteins myosin and actin, respectively. The precise arrangement of these filaments, which run parallel to the longitudinal axis of the cell, forms the fundamental force-generating units known as sarcomeres, which are aligned end-to-end. Each myofibril is surrounded by the sarcoplasmic reticulum (SR), which serves as a reservoir for calcium ions (Ca^{2+}). The SR is closely associated with another structure called the transverse tubules (T-tubules), which are connected to the sarcolemma and penetrate deep into the cell interior. Figure 2.1 illustrates the main structural components of skeletal muscle, from the whole muscle down to the sarcomere level.

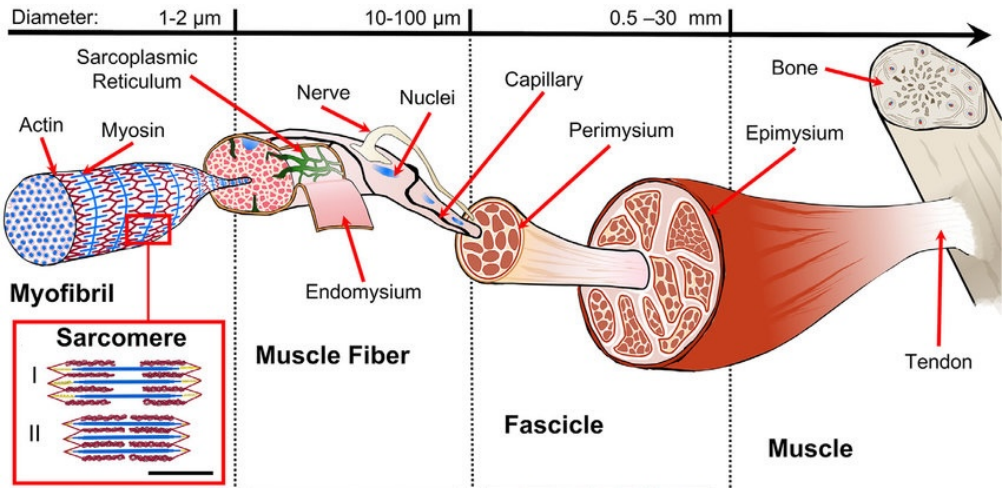

Figure 2.1: Structural organization of skeletal muscle, adapted from [9]. Sarcomere morphology and sliding mechanism (scale bar: 0.5 nm). Actin (red), myosin (blue), and titin (yellow) filaments are shown in the relaxed state (I) and during contraction (II). The jagged sides represent the Z-lines, while the central space without actin filaments corresponds to the H zone.

Each thick filament is composed of hundreds of myosin molecules, each consisting of two twisted subunits. Each subunit has a tail and an enlarged head that protrudes laterally. The myosin heads, also known as cross-bridges, are responsible for generating the movement that drives muscle contraction. These heads contain two critical sites: one that binds to actin and another with enzymatic activity, capable of hydrolyzing ATP. The fundamental components of each thin filament are actin monomers, each possessing a binding site for myosin. These actin monomers polymerize end-to-end, forming filamentous structures that intertwine into a double-helical arrangement, giving rise to the actin filaments within the thin filaments. Two regulatory proteins, troponin and tropomyosin, are present on the thin filament and play a key role in initiating or inhibiting contraction. Similarly, thick filaments are also associated with additional proteins, the most important being titin - an exceptionally elastic protein that ensures the proper alignment of thick filaments relative to thin filaments.

2.1.2 Mechanism of force generation

The thick and thin filaments slide past each other, causing the sarcomeres to shorten, which in turn shortens the myofibrils. This process is mirrored in the muscle fibers and ultimately leads to the shortening of the entire muscle. The mechanism by which the thick and thin filaments slide past each other during muscle contraction is known as the cross-bridge cycle. At the core of this mechanism is an oscillatory motion - back and forth - of the cross-bridges between myosin and actin, driven by the energy released from ATP hydrolysis. This activity is coupled with the cyclical alternation between the binding and detachment of the cross-bridges from the thin filaments, which results in the pulling of the thin filaments toward the center of the sarcomere. This process is schematically illustrated in Figure 2.2, which depicts the cross-bridge cycle underlying sarcomere shortening.

The cyclical interaction between myosin and actin filaments constitutes the fundamental mechanical basis of muscle contraction. However, such molecular events do not occur spontaneously; they must be triggered by electrical signals that originate from the nervous system. In skeletal muscle, each muscle fiber receives signals from a single motor neuron, which branches out to innervate multiple fibers. An action potential that develops in a motor neuron triggers the release of acetylcholine, which binds to receptors on the neuromuscular junction of the muscle fiber. This generates an electrical signal (end-plate potential), which leads to the initiation of an action potential that propagates very rapidly along the sarcolemma in both directions (at 2 to 6 m/s in humans) and then much more slowly (0.3 m/s) [2] throughout the t-tubular system. The rapid sarcolemmal propagation is necessary to synchronously activate all parts of the muscle fiber to produce a useful contraction, and the conduction in the tubular system can be much slower

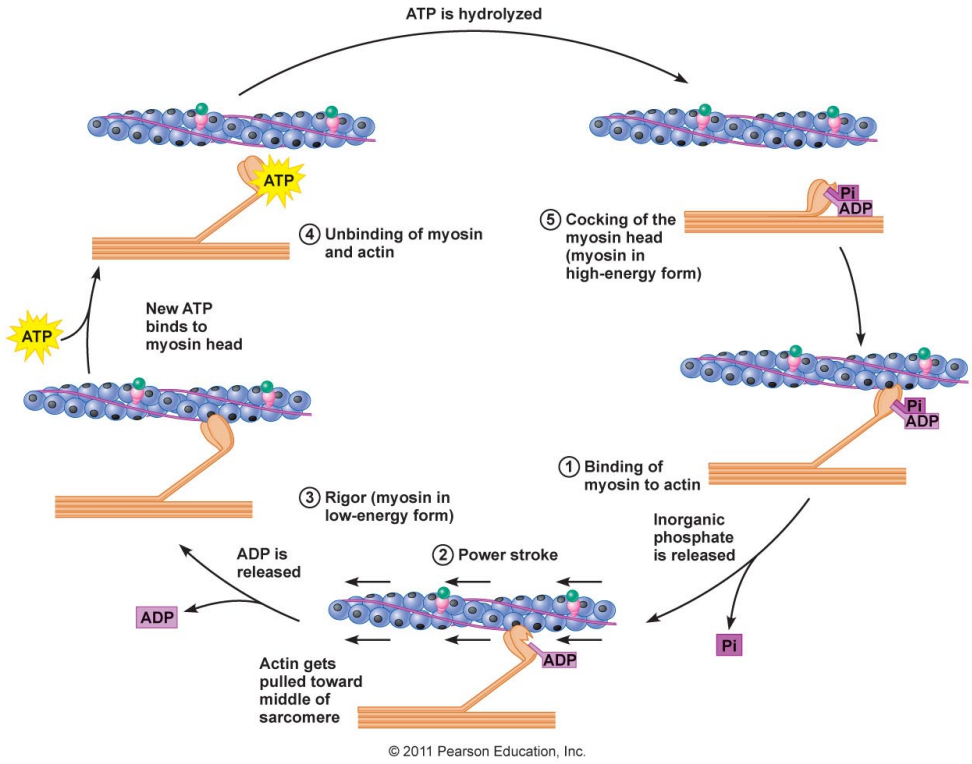

Figure 2.2: Schematic representation of the cross-bridge cycle underlying muscle contraction, as illustrated in [8]. Myosin heads attach to actin filaments, perform a power stroke fueled by ATP hydrolysis, and then detach and re-cock, enabling repeated cycles of filament sliding and sarcomere shortening.

because of the small distances involved. This action potential stimulates the release of (Ca^{2+}) from the SR, which binds to troponin, exposing the binding sites on actin for myosin. Consequently, the cross-bridge cycle begins, and the muscle fibers contract. Once the action potential ceases, (Ca^{2+}) is actively reabsorbed into the SR lumen, and tropomyosin blocks the binding sites for myosin, allowing the muscle fibers to relax.

As seen, calcium plays a key role as the signal that initiates the cross-bridge cycle and, therefore, muscle contraction. The force of contraction depends on the amount of calcium ions present in the cytosol: a higher concentration of calcium corresponds to more binding sites on actin available for myosin, which in turn leads to more cross-bridge cycles. A muscle cell ceases contraction when it no longer receives signals from the motor neuron, and as a result, no more action potentials are generated along the sarcolemma.

2.1.3 Regulation of muscle force and muscle fiber characteristics

As briefly mentioned in Subsection 2.1.2, each skeletal muscle fiber is innervated by a single motor neuron, which branches out to activate multiple fibers. Consequently, the action potential of a motor neuron leads to the synchronous contraction of all the muscle fibers it innervates, making it impossible to stimulate an individual fiber in isolation. This functional entity, consisting of the motor neuron and all the fibers under its control, is referred to as a motor unit. Figure 2.3 schematically illustrates the organization of two motor units.

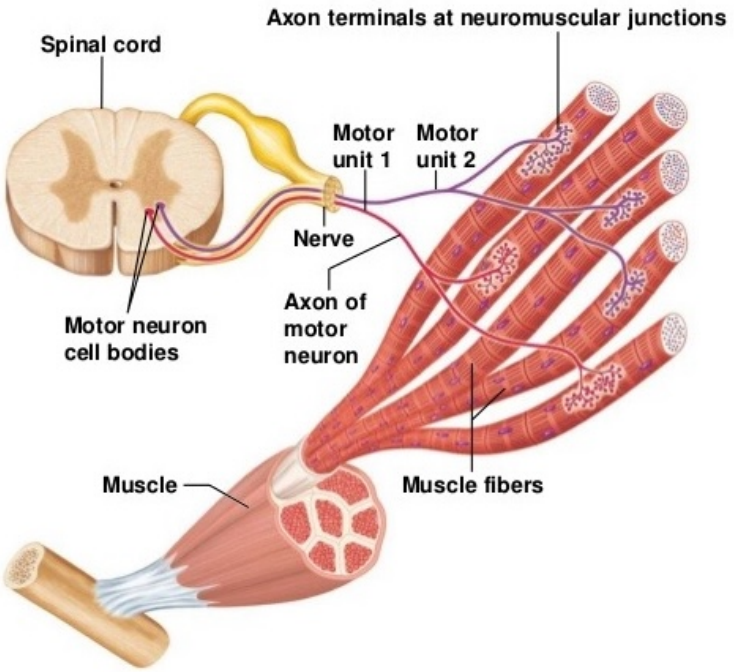

Figure 2.3: Schematic representation of two motor units. A single motor neuron branches to innervate multiple muscle fibers, which contract simultaneously in response to an action potential.

The force generated by a muscle depends on two factors:

1. The force developed by each individual muscle fiber, which, in turn, depends on:

   - Stimulation frequency;
     in a muscle fiber, numerous action potentials can occur within the time it takes for a full contraction to complete. When a muscle is repetitively

stimulated, such that the subsequent action potential arrives before the previous contraction has finished, the twitches overlap, generating a force greater than that produced by a single twitch. This phenomenon is called summation, and it occurs whenever the twitches are frequent enough that the removal of calcium from the cytosol cannot occur as quickly as it is released from the SR. For relaxation to occur, the calcium ions must be removed; therefore, the muscle fiber cannot relax between contractions. Figure 2.4 depicts the progressive increase in force from a single twitch to summation, unfused tetanus, and finally smooth tetanus, which represents the maximal sustained contraction.

- Diameter of muscle fibers;

  a muscle that has a higher number of sarcomeres arranged in parallel can generate greater force than a muscle with fewer sarcomeres. Since the number of thick and thin filaments per unit of cross-sectional area does not significantly vary from one muscle to another, it follows that the diameter of the muscle fiber is a key variable in determining contractile force. The larger the fiber diameter, the greater the cross-sectional area, and the more force can be generated.

- Variation in the length of muscle fibers.

  Each muscle fiber has an optimal length at which it can produce maximum force, when the maximum number of myosin cross-bridges contribute to force generation. When a fiber is either longer or shorter than its optimal length, its ability to generate force decreases because changes in the muscle length lead to changes in the length of the individual sarcomeres, which in turn reduces their ability to develop force.

2. The number of contracting muscle fibers.

   The nervous system exerts most of its control over muscle strength by varying the number of motor units activated; an increase in the number of active motor units is known as recruitment. Within a muscle, the fibers belonging to a given motor unit are intermixed with others that belong to different motor units. Not all motor units are identical: they often differ in size, as some contain a higher number of muscle fibers, while others have relatively fewer. Since a muscle can contain hundreds of motor units, muscle tension can be adjusted across a significant range simply by varying the number of active motor units. Some motor units are primarily composed of small muscle fibers, while others are made up of larger fibers, which tend to have a greater number of fibers as well. According to Henneman's size principle, when a muscle is used to generate moderate forces, typically only the smaller motor units are recruited. As higher forces are required, larger motor units are recruited. Larger motor units are

controlled by motor neurons with larger cell bodies and axon diameters than average, while smaller motor units are governed by motor neurons with smaller cell bodies and axons. The larger neurons face more difficulty in reaching the threshold to generate an action potential, so when a gradually increasing synaptic input reaches a group of motor neurons, the smaller ones fire first, followed by the larger ones. Moreover, when contraction is sustained over time, motor units are activated asynchronously - when one becomes active, another ceases its activity. This ensures that the total muscle force remains consistent, preventing any of the active motor units from becoming overloaded.

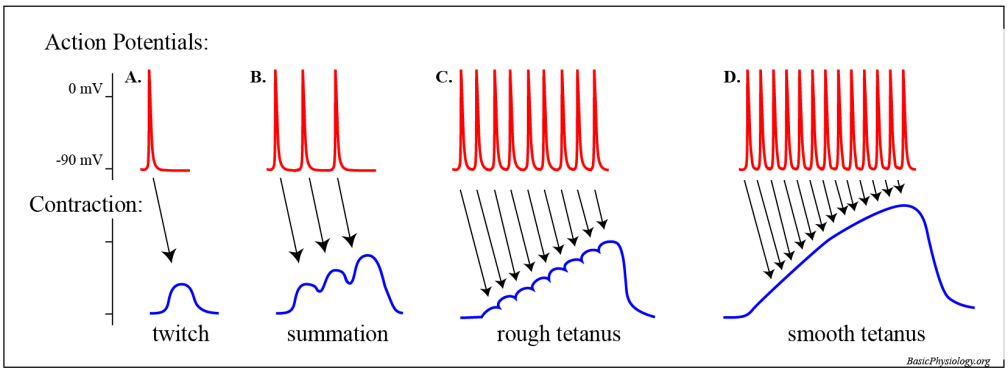

Figure 2.4: Representative force responses of skeletal muscle to different patterns of stimulation. (A) A single stimulus evokes a brief, isolated contraction known as a twitch. (B) When stimuli are delivered before the muscle has fully relaxed, the individual contractions begin to summate, resulting in a higher overall force. (C) With repeated, rapid stimulation, the individual twitches merge into an unfused (or rough) tetanus. (D) At sufficiently high frequencies, the contractions fully fuse into a smooth tetanus, characterized by a sustained plateau of maximal force.

2.1.4 Muscle metabolism and energy sources during exercise

Muscle contraction requires a continuous supply of ATP, a high-energy molecule that fuels cellular processes. However, the ATP stored in muscle fibers is limited and must be rapidly regenerated to sustain activity. To achieve this, the body relies on three interconnected energy systems: the phosphagen system (anaerobic alactic), the glycolytic system (anaerobic lactic), and the oxidative system (aerobic). At the onset of contraction, the phosphagen system provides an immediate but short-lived ATP source by utilizing phosphocreatine (PCr) reserves. This reaction ensures energy availability while other metabolic pathways activate. As exercise

continues, the glycolytic system becomes more prominent, breaking down glucose anaerobically to produce ATP, though at the cost of lactate accumulation. For prolonged activity, the oxidative system takes over, utilizing oxygen to metabolize carbohydrates and fats, enabling sustained ATP production [10]. While these systems were once thought to function sequentially, current research indicates that they operate simultaneously, with their relative contribution depending on exercise intensity and duration. For example, anaerobic and aerobic metabolism reach a balance approximately 75 seconds into maximal exertion, as shown in Figure 2.5. At rest, ATP demand is low, but upon stimulation, it increases immediately. Although oxidative phosphorylation and glycolysis contribute to ATP resynthesis, they require a few seconds to reach optimal efficiency. In the meantime, the phosphagen system plays a crucial role by transferring a phosphate group from PCr to ADP, rapidly forming ATP. Although this mechanism is limited in duration, it bridges the gap until slower but more sustainable pathways become dominant. The choice of ATP production pathway is influenced by exercise intensity and oxygen availability. During low-intensity exercise, oxidative phosphorylation predominates due to an adequate oxygen supply. However, as intensity increases, reliance shifts towards anaerobic glycolysis, which can generate ATP quickly but leads to metabolite accumulation and fatigue.

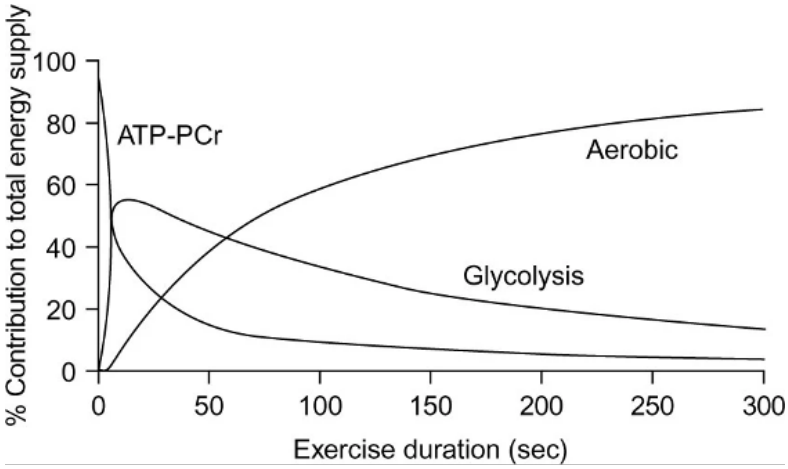

Figure 2.5: Relative energy system contribution to the total energy supply for any given duration of maximal exercise, taken from [10]

2.1.5 Target muscle in this study and isometric contraction

This thesis focuses on the assessment of muscle fatigue in the extensor digiti minimi (EDM) during isometric contractions, that is, when the muscle develops mechanical tension while maintaining a constant length. The EDM is the primary extensor of

the little finger and, like most skeletal muscles, it is composed of a mixture of fiber types.

Muscle fibers can be classified as slow or fast based on their contraction speed, which is primarily determined by the expression of myosin heavy chain (MHC) isoforms. Type I fibers have the slowest cross-bridge cycling and shortening velocity, while type IIa fibers are intermediate, and type IIx/b fibers are the fastest. However, shortening velocity can also vary between fibers with the same MHC expression, indicating the influence of additional factors. Fibers can also be categorized as glycolytic or oxidative, based on their primary ATP production mechanism. Glycolytic fibers have a high concentration of glycolytic enzymes, allowing them to rapidly generate ATP via substrate-level phosphorylation. In contrast, oxidative fibers rely on mitochondria-rich oxidative phosphorylation for ATP production but contain lower concentrations of glycolytic enzymes. The rate of ATP consumption also differs, as fast MHC isoforms utilize ATP at a higher rate than slow isoforms. Another key ATP-consuming component in muscle is the sarcoplasmic reticulum Ca^{2+} pump (SERCA), with SERCA1 found in fast fibers and SERCA2 in slow fibers, with a higher pump density in fast fibers. Structurally, oxidative fibers are smaller in diameter, well-vascularized, and contain myoglobin, which enhances oxygen storage and gives them a red appearance. In contrast, glycolytic fibers are larger, have fewer capillaries, lack myoglobin, and appear white. While slow type I fibers are generally more fatigue-resistant than fast type II fibers, this is mainly due to their higher mitochondrial density and oxidative capacity, rather than just their MHC isoform expression. Based on these distinctions, three main types of muscle fibers have been identified, as shown in Table 2.1.

Characteristics	**Type I - slow oxidative**	**Type IIa - fast oxidative**	**Type IIb - fast glycolytic**
Contractile velocity	Low	Intermediate	Fast
Aerobic (oxidative) capacity	High	High	Low
Anaerobic (glycolytic) capacity	Low	Intermediate	High
Fiber diameter	Small	Intermediate	Large
MU dimension	Small	Intermediate	Large
Ability to generate force	Low	Intermediate	High
Fatigue resistance	High	Intermediate	Low

Table 2.1: Classification of skeletal muscle fiber types. The table summarizes the main characteristics of human skeletal muscle fibers, including contraction velocity, primary metabolic pathway, fiber diameter and fatigue resistance.

During sustained isometric contractions, motor unit recruitment follows a hierarchical pattern: slow oxidative fibers are activated first, followed by fast oxidative fibers, and finally, under conditions of higher force demand or fatigue, fast glycolytic fibers. This orderly recruitment reflects the activation of smaller motor units before

larger ones. Since fast glycolytic fibers are highly susceptible to fatigue, their progressive involvement plays a key role in the onset of muscle fatigue, a phenomenon analyzed in the present work. Although relatively few studies have examined the EDM in isolation, histological investigations of the extensor digitorum communis (EDC), which also contributes to little finger extension, and of smaller extensor muscles suggest that the EDM displays a balanced distribution of fiber types, without a strong predominance of either slow or fast fibers. Such a composition appears functionally reasonable, as the little finger requires both precision and speed.

2.2 Muscle Fatigue

Muscle fatigue refers to the decline in the ability of skeletal muscle to generate force or power during sustained activity. This section outlines the main metabolic changes leading to fatigue, the compensatory mechanisms at the neuromuscular level, and the principal ways in which fatigue can be classified.

2.2.1 Metabolic changes and fatigue mechanisms

Muscle fatigue arises from complex metabolic alterations that progressively impair contractile function. During sustained activity, the muscle undergoes significant biochemical changes, including the accumulation of metabolic byproducts and the depletion of key energy substrates. These factors disrupt normal excitation-contraction coupling, reducing force output and slowing muscle relaxation. As well explained in the paper by Allen et al. [2], the primary contributors to fatigue include inorganic phosphate accumulation, changes in lactate and hydrogen ion (H^+) levels, alterations in ATP and magnesium ion (Mg^{2+}) concentrations, and glycogen depletion.

1. Inorganic phoshate (Pi) accumulation;

   one of the earliest and most significant metabolic disturbances during muscle fatigue is the accumulation of Pi, a byproduct of ATP hydrolysis. Elevated Pi concentrations interfere with calcium release from the sarcoplasmic reticulum, reducing the availability of Ca^{2+} for muscle contraction. Additionally, Pi has been shown to directly inhibit myofibrillar ATPase activity, slowing cross-bridge cycling and decreasing force production. This accumulation is particularly detrimental in repetitive contractions.

2. Lactate and hydrogen ions (H^+);

   during high-intensity exercise, anaerobic metabolism leads to an increased

production of lactate and H^+. The accumulation of H^+ contributes to intracellular acidosis, which disrupts muscle function by impairing calcium binding to troponin and reducing the efficiency of actin-myosin interactions. While lactate itself was historically believed to cause fatigue, current evidence suggests that its primary role is to act as a buffer, delaying the onset of acidosis rather than directly impairing contraction. However, excessive H^+ levels still compromise force generation and slow relaxation, both of which are critical for repetitive movements.

3. ATP and magnesium ions (Mg^{2+});

   ATP availability is essential for muscle contraction, and its depletion is a hallmark of fatigue. As ATP levels drop, Mg^{2+} concentration in the cytoplasm increases because ATP normally binds Mg^{2+} to form ATP-Mg^{2+} complexes. Elevated Mg^{2+} can further inhibit calcium release from the sarcoplasmic reticulum, exacerbating the decline in contractile force. Although complete ATP depletion is rare, localized ATP shortages at the myofibrillar level can still impair muscle performance.

4. Glycogen depletion.

   Glycogen serves as the primary energy reserve for prolonged muscle activity. As exercise continues, glycogen stores become depleted, limiting ATP resynthesis through glycolysis. This depletion is particularly relevant in sustained contractions, where muscle fibers rely heavily on carbohydrate metabolism. Once glycogen availability declines, the muscle's ability to sustain force production is significantly reduced, contributing to fatigue.

2.2.2 Neuromuscular compensatory mechanisms

During sustained or intense muscular activity, fatigue leads to a progressive decline in performance. To counteract this reduction and preserve force output as long as possible, the neuromuscular system adopts several compensatory strategies. These mechanisms act at the level of motor unit recruitment and firing behavior:

- Increased motor unit firing rate;

  the central nervous system raises the discharge frequency of active motor units, enhancing temporal summation and thereby sustaining force production.

- Recruitment of additional motor units;

  as fatigue progresses, previously inactive motor units are recruited, providing fresh contractile fibers to support the task.

- Rotation or substitution of active motor units.

  Some motor units can be temporarily deactivated and replaced by others, allowing partial recovery and delaying exhaustion of individual fibers.

These compensatory strategies are crucial for maintaining performance in the presence of fatigue, although they can only temporarily offset the progressive decline in muscular efficiency.

2.2.3 Classifications of muscle fatigue

Muscle fatigue is a complex and multifactorial phenomenon that can be classified according to different criteria, depending on the site of origin, duration, or nature of the fatigue experienced. These distinctions are essential to understand the underlying mechanisms and to select appropriate monitoring techniques and intervention strategies. During voluntary contractions, muscle activation originates in the motor cortex and travels through descending pathways to reach the spinal cord, where lower motor neurons are activated. These neurons transmit action potentials along their axons to the neuromuscular junction, ultimately triggering muscle fiber contraction. Fatigue can occur at any level along this pathway and is broadly categorized as either central or peripheral. These two components, and their main sites of action, are schematically illustrated in Figure 2.6.

Central fatigue refers to impairments occurring at the supraspinal and spinal levels - that is, changes within the central nervous system, from the motor cortex to the spinal cord, that lead to a decline in voluntary muscle activation. It is associated with reduced firing rates and synchronization of motor units, and a reduced drive from the motor cortex. Peripheral fatigue, on the other hand, involves processes distal to the neuromuscular junction, including metabolic and biochemical changes within the muscle that impair excitation-contraction coupling and force generation [2]. The relative contribution of these two components is task-dependent, with one mechanism possibly dominating over the other depending on the type, intensity, and duration of the activity [1, 11].

Another commonly used classification is based on the duration of the fatigue. Acute fatigue develops over a short period and is typically reversible with rest or appropriate recovery strategies. It is commonly observed following intense physical activity. In contrast, chronic fatigue refers to a persistent sense of tiredness or lack of energy lasting for months, which does not resolve with rest. This form of fatigue may be associated with underlying medical conditions or syndromes and often requires clinical evaluation [7].

Fatigue can also be classified according to its nature. Mental fatigue involves cognitive or perceptual aspects, such as reduced concentration, alertness, or motivation. Physical fatigue refers specifically to impairments in motor performance

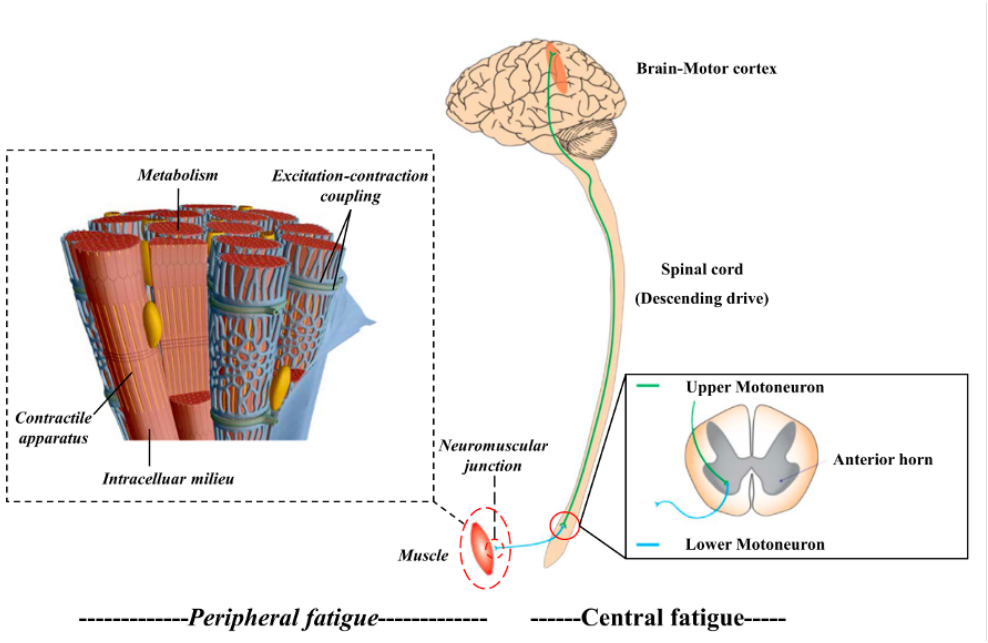

Figure 2.6: Central fatigue is associated with a decrease in the efferent drive from the motor cortex, leading to a lower motoneuron discharge rate. Peripheral fatigue refers to a decline in muscle output caused by alterations in the electrochemical and mechanical processes occurring downstream of the neuromuscular junction. Adapted from [1].

and includes both central and peripheral components [1, 7]. Although mental and physical fatigue are conceptually distinct, they may interact with one another. For example, prolonged cognitive load may indirectly affect motor performance, and vice versa.

2.3 Non-invasive techniques for muscle fatigue monitoring

Imaging has become an indispensable tool in the study of muscle physiology and pathology, offering non-invasive access to both structural and functional characteristics of muscle tissue. In the context of muscle fatigue, imaging enables the monitoring of dynamic changes in muscle architecture, perfusion, and oxygenation during exercise. Techniques such as US imaging provide information on muscle deformation and contractile behavior, while PAI offers insight into hemoglobin saturation and microvascular responses. Combined with neuromuscular data from HD-sEMG, these approaches allow a comprehensive assessment of the relationship

between electrical activation, mechanical output, and vascular/metabolic status. To this end, the following subsections will briefly introduce each technique, outlining their respective strengths and limitations. As will become evident from the following descriptions, the complementary nature of these techniques supports their combined use for a more complete assessment of muscle fatigue.

2.3.1 Ultrasound

Ultrasound (US) imaging uses mechanical sound waves with frequencies above the audible range ($\geq$20 kHz), typically between 2 and 10 MHz in medical applications, to view inside the body. Modern ultrasound devices rely on piezoelectric crystals embedded in the transducer to convert electrical energy into mechanical (acoustic) waves [1]. These waves propagate through tissues and are partially reflected at interfaces where differences in acoustic impedance (z) occur - a property defined by the tissue's density (ρ) and the speed of sound in the medium (v) as follows

$$z = \rho v \tag{2.1}$$

It can be observed that even very different tissues and organs may exhibit similar values of density and acoustic impedance, as is the case for blood and muscle. The values for the most relevant tissues are summarized in Table 2.2 below, providing context for the ultrasound contrast observed in muscle imaging.

Tissue	**Density (kg/m^3)**	**Speed of sound (m/s)**	**Acoustic impedance (10^6 kg/m^2/s)**
Air	1.2	330	0.0004
Water	1000	1480	1.48
Blood	~1050-1060	~1570-1584	~1.65-1.68
Liver	1060	1550	1.64
Muscle	1080	1580	1.70
Fat	952	1459	1.38
Brain	994	1560	1.55
Kidney	1038	1560	1.62
Lung	400	650	0.26
Soft tissue (mean)	1060	1540	1.63
Bone	1912	4080	7.80

Table 2.2: Typical values of density, speed of sound, and acoustic impedance for different tissues.

The ultrasound image represents a mapping of all the acoustic impedance discontinuities encountered by the ultrasound waves as they propagate through the tissues. Thus, by emitting a sequence of US pulses along a predefined scan line and capturing the returning echoes, an image that maps the spatial distribution of

acoustic impedance discontinuities within the irradiated tissues can be reconstructed. The transducer converts the returning waves back into electrical signals, which are then processed to generate images that reveal the structural properties of the tissues under investigation.

US imaging can be performed in various modes. In this study, brightness-mode (B-mode) ultrasound was employed, as it allows for two-dimensional imaging of the muscle, whereas amplitude-mode (A-mode), which measures echoes along a single line, was not used. For B-mode ultrasound, parameters such as muscle thickness, cross-sectional area, pinnation angle, and fibre length are frequently employed to assess fatigue levels [1]. In the context of this study, US imaging serves primarily as a morphological reference, providing a structural map on which photoacoustic images are subsequently overlaid. This approach enables the integration of functional information from photoacoustic imaging with the anatomical context provided by US. The main advantages of US include its safety due to non-ionizing radiation, high temporal resolution, and the ability to target specific muscles of interest. Limitations include a restricted field of view and reduced image quality at greater depths, though these are not critical for the present application.

2.3.2 Photoacoustic Imaging

PAI is a hybrid imaging modality that combines optical illumination with US detection. A nanosecond pulsed laser (pulse duration <10 ns) is commonly used to illuminate the tissue. When the light is absorbed by tissue chromophores, such as hemoglobin in blood vessels, melanin, lipid or water, the optical energy is converted into heat, causing a minimal, slight and rapid temperature rise (on the order of a few millidegrees). This temperature increase induces thermoelastic expansion, which generates acoustic waves that are subsequently detected by ultrasonic transducers [12, 13, 14]. From these acquired PA signals, PA images are obtained using appropriate image reconstruction algorithms which in turn provide the structural/functional information of the tissue of interest [13, 15]. A schematic representation of the technique is shown in Figure 2.7 below.

Originally conceptualized over a century ago, the photoacoustic effect found its first major biomedical applications in the early 2000s, driven by advances in laser technologies and ultrasound detection systems. In recent years, PAI has been increasingly applied in various biomedical domains, including breast imaging, dermatology, vascular diagnostics, gastrointestinal assessment, adipose tissue analysis, neurological research, and more recently, muscle and metabolic physiology [12, 13]. While many of these applications are still under active investigation, several have already progressed toward clinical adoption, highlighting the translational potential of PAI. Although it remains primarily a research modality in muscular studies, PAI's clinical integration has already begun in domains such as breast cancer diagnostics

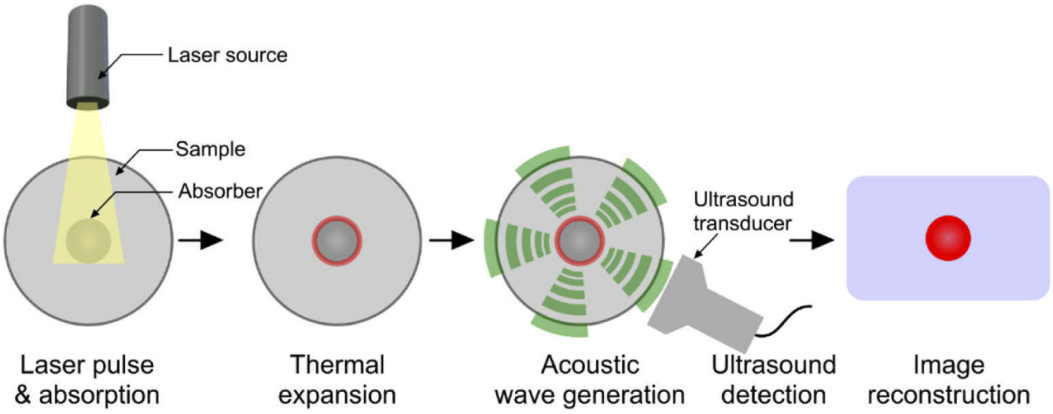

Figure 2.7: Overview of PA signal generation and image reconstruction, taken from [15]. A short laser pulse heats the absorber, causing thermoelastic expansion and emission of acoustic waves. These are detected by an ultrasound probe and processed to form the PA image.

(e.g., Imagio), vascular visualization, and dermatologic assessment, supported by CE-marked systems like MSOT Acuity and RSOM [12, 16, 17]. Central to these clinical advances is the unique imaging mechanism of PAI, which leverages the fact that endogenous chromophores, such as hemoglobin and melanin, have distinct absorption spectra. By using multiple laser wavelengths, PAI enables the selective excitation of these chromophores, facilitating their identification and quantification. This spectroscopic capability allows for the extraction of rich functional data about tissue composition, oxygenation status, and metabolic changes [12].

Several prior studies [18, 19, 20, 21, 22, 23, 24, 25] have employed multiwavelength photoacoustic imaging to investigate skeletal muscle, with a primary focus on quantifying different forms of hemoglobin (oxygenated, deoxygenated, and total). These investigations demonstrate PAI's ability to monitor real-time oxygenation dynamics, thus providing key insights into muscle function, fatigue, and pathophysiological states.

Why PAI instead of NIRS?

An important methodological consideration concerns the choice of PAI over near-infrared spectroscopy (NIRS) or other purely optical techniques. Several studies [13, 19, 20, 21, 24] have highlighted the limitations of light-based methods and the advantages offered by PAI. The main limitation of optical techniques such as NIRS and diffuse optical tomography (DOT) lies in the strong scattering and absorption of photons in biological tissues. While NIRS provides valuable information on

tissue oxygenation, its effective imaging depth is limited. DOT can partially mitigate this issue but still suffers from low spatial resolution (typically 5-10 mm). Furthermore, NIRS signals often contain uncertain contributions from both muscle and superficial tissues (particularly subcutaneous fat and skin), which complicates the reliable separation and quantification of hemoglobin species. In contrast, PAI overcomes these limitations by relying on US detection. Acoustic waves experience approximately 1000 times less scattering than photons in tissue [12], enabling deeper penetration with minimal distortion. As a result, PAI achieves greater imaging depth and spatial resolution, while still preserving sensitivity to hemoglobin oxygenation dynamics.

Spectral Unmixing

PA images representing the distribution of spectrally-distinct chromophores are generally obtained with a two-step procedure. In a first step, optoacoustic tomographic images are reconstructed from the pressure signals generated by absorption of short laser pulses. In the second step, spectral unmixing algorithms are imposed on the images acquired at different excitation wavelengths in order to map the distribution of different absorbing substances present in the tissue [26]. This step is crucial because, while PAI excels in mapping spatial variations in optical absorption, it does not inherently distinguish between specific chromophores. This limitation is addressed through spectral unmixing, a mathematical technique that deciphers multi-wavelength PAI data by referencing the known absorption spectra of target biomolecules. Endogenous chromophores such as oxygenated (HbO_2) and deoxygenated hemoglobin (Hb), lipids, and water exhibit characteristic spectral profiles, allowing their contributions to the total signal to be resolved and quantified. In muscle imaging, this is particularly valuable for tracking dynamic changes in oxygenation during contraction or ischemia-reperfusion events [21]. Spectral unmixing algorithms, ranging from linear model-based approaches to advanced machine learning techniques, enable the generation of functional maps that provide insight into tissue oxygenation, perfusion, and metabolic state [12, 27].

2.3.3 High-Density Surface Electromyography

Motor commands originating in the central nervous system activate motor neurons, which recruit motor units within the muscle. The resulting electrical activity generates biopotentials that can be detected at the skin surface as electromyographic (EMG) signals. The EMG signal is the result of the asynchronous summation of the electrical potentials from multiple motor units (Figure 2.8). Surface EMG (sEMG) is a common method used for acquiring signals from muscles during both static and dynamic contractions and can be recorded from various parts of the body by

placing electrodes on the skin surface above the target muscle [1, 5].

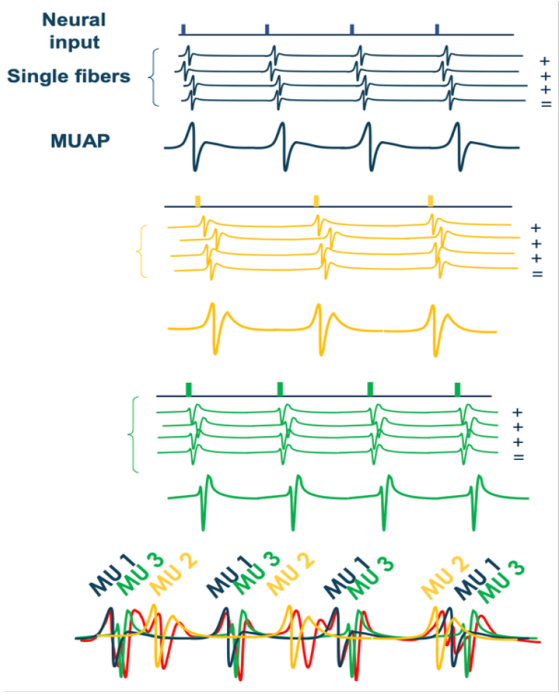

Figure 2.8: Illustration of the contribution of neural input and single muscle fibers to motor unit action potentials (MUAPs), showing how the activation of multiple motor units (MU1, MU2, MU3) combines to form the composite EMG signal.

HD-sEMG builds on conventional sEMG by using multipolar electrodes arranged in arrays or matrices, allowing signal acquisition from a much wider area of the target muscle [1]. One of the main advantages of HD-sEMG is its ability to capture detailed spatial information. While standard sEMG provides only the combined activity of all motor units, HD-sEMG enables the differentiation of signals from individual motor units. This allows for the extraction of richer data, such as identifying innervation zones, estimating action potential, conduction velocity (CV), locating tendons, and even decomposing individual MUAPs using advanced algorithms [28]. A major application of HD-sEMG is in the study of muscle fatigue. The primary myoelectric marker of fatigue is a decrease in conduction velocity, which reflects the propagation speed of depolarization along the muscle fibers [29]. CV is estimated by measuring the delay between signals recorded at fixed distances along the fibers [30]. In fatigue analysis, both frequency-domain and time-domain parameters are typically combined to characterize the process. At the onset of a sustained contraction, the EMG signal displays a characteristic spectral profile.

As fatigue sets in and conduction velocity slows, the power spectrum shifts and compresses toward lower frequencies. This shift is quantified using mean frequency (MNF) and median frequency (MDF). Although these are spectral parameters calculated in the frequency domain, they are usually plotted as a function of time to track the fatigue progression. In the time domain, parameters such as average rectified value (ARV) and root mean square (RMS) amplitude tend to increase with fatigue, reflecting changes in signal amplitude. These descriptors, widely used in fatigue studies, can be selected and combined depending on the experimental protocol and the specific aspects of muscle function under investigation.

Chapter 3

Materials and Methods

This chapter describes the experimental setup and the methodological framework employed in this thesis. First, the instrumentation and acquisition procedures are presented, including the integration of US, PAI and HD-sEMG. Then, the experimental protocol adopted for data collection is outlined. Finally, the data processing steps are detailed, covering image reconstruction, spectral unmixing, and EMG feature extraction.

3.1 Experimental Setup

3.1.1 Imaging hardware

US and PA imaging were performed using a Verasonics Vantage 256 research platform equipped with an L11-5v linear array transducer, featuring 128 elements and a center frequency of 7.8 MHz. The Verasonics system, connected via PCIe cable to a host computer running MATLAB-based control software, provided a flexible platform for transmitting, receiving, and processing US and PA data. Imaging sequences were defined through MATLAB scripts, enabling synchronized control of acquisition parameters and laser triggering for PA imaging, as detailed in Section 3.1.2. The Verasonics VSX interface, launched via MATLAB, displayed reconstructed US and PA images in real-time. This interface allowed runtime adjustments of key parameters, such as time gain control, transmission voltage, and acquisition settings, synchronized with the hardware through periodic hand-offs between VSX and the RunAcq module. The RunAcq function transmitted all parameters to the hardware, collected raw data into the RcvBuffer variable, and returned reconstructed images to the VSX interface for display. Signal sampling was set to 31.2 MHz, four times the transducer's center frequency, to meet the Nyquist criterion and ensure accurate digitization. After each session, raw US and PA data

were stored for offline processing. The system architecture for US/PA sequencing is illustrated in Figure 3.1. US imaging provided morphological references for anatomical structures, while PA imaging enabled the assessment of tissue optical absorption for functional metrics, such as oxygenated hemoglobin levels (HbO_2), as described in Section 3.3.3.

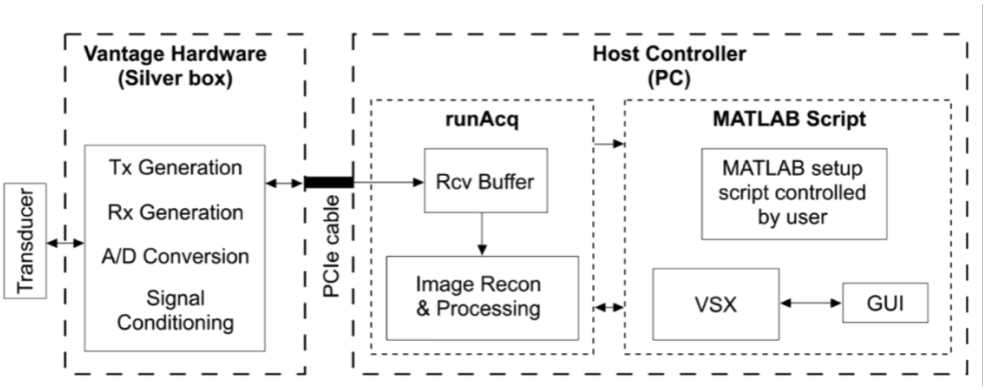

Figure 3.1: Vantage system architecture and data acquisition sequencing, taken from [15].

3.1.2 Laser source and wavelength configuration

The photoacoustic signal was generated by illuminating the tissue with pulsed laser light and detecting the resulting acoustic waves with the US transducer. Illumination was provided by an Opotek Phocus Mobile SE system, a tunable laser source based on ring-cavity optical parametric oscillator technology. This configuration enables the generation of high pulse energies across the near-infrared spectrum, providing sufficient penetration depth for biological tissues. The laser delivered wavelengths in the range of 690-950 nm through two flexible optical fiber bundles mounted laterally on either side of the transducer The experimental setup is shown in Figure 3.1. This illumination geometry ensured uniform exposure of the region of interest while avoiding obstruction of the acoustic detection path. For each acquisition, the actual pulse energy was recorded via the StarLab software (version 2.40, Build 8) and later used to normalize the photoacoustic measurements.

3.1.3 Load cell measurement and force feedback system

A load cell integrated into a custom wooden support continuously recorded the force applied by the little finger, which was pushed upwards against a resistance. The system provided real-time feedback, allowing subjects to maintain the target force

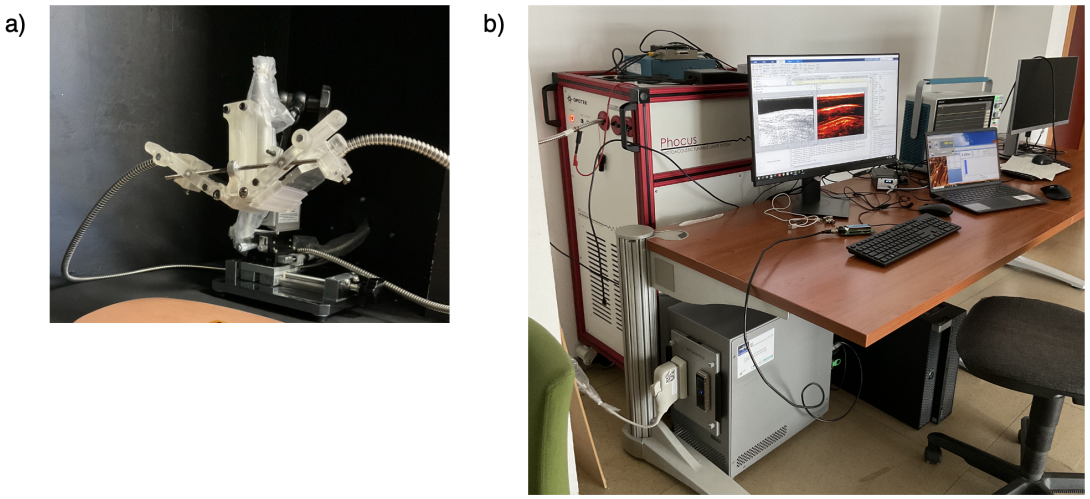

Figure 3.2: a) Experimental setup showing the ultrasound transducer with bifurcated fiber optic illumination. b) Experimental setup for US and PA imaging. The Verasonics Vantage 256 research platform is positioned under the desk (left), connected to a host computer (center) running the MATLAB-based VSX interface, which displays real-time US and PA images on the monitor. The Phocus Mobile Laser System (rear) provides the laser source for PA imaging, controlled by a separate computer (right). The setup includes the L11-5v linear array transducer (not visible in this view) mounted during experiments.

steadily throughout the acquisition (Figure 3.3). This setup ensured controlled and repeatable force output, forming a reliable foundation for the subsequent acquisition of imaging and electrophysiological data.

3.1.4 HD-sEMG acquisition system and electrode grid placement

HD-sEMG signals were acquired using the MEACS system, a CE-marked, modular, and wireless device specifically designed for the study of neuromuscular activity by the LISiN reasearch group at Politecnico di Torino [31, 32]. A single 32-channel module, corresponding to the electrode grid applied on the target muscle, was employed in this work. Signals were sampled at 2048 Hz with 16-bit resolution, an ADC dynamic range of 2.4 V, and a front-end gain of 192 V/V. The system is fully wireless and battery-powered, with electrode grids connected directly to the MEACS probe, minimizing connecting cables and thereby reducing triboelectric noise and movement artifacts. A General-purpose Acquisition Module (GAM) was used to acquire and synchronize the load cell signal with the HD-sEMG data, ensuring

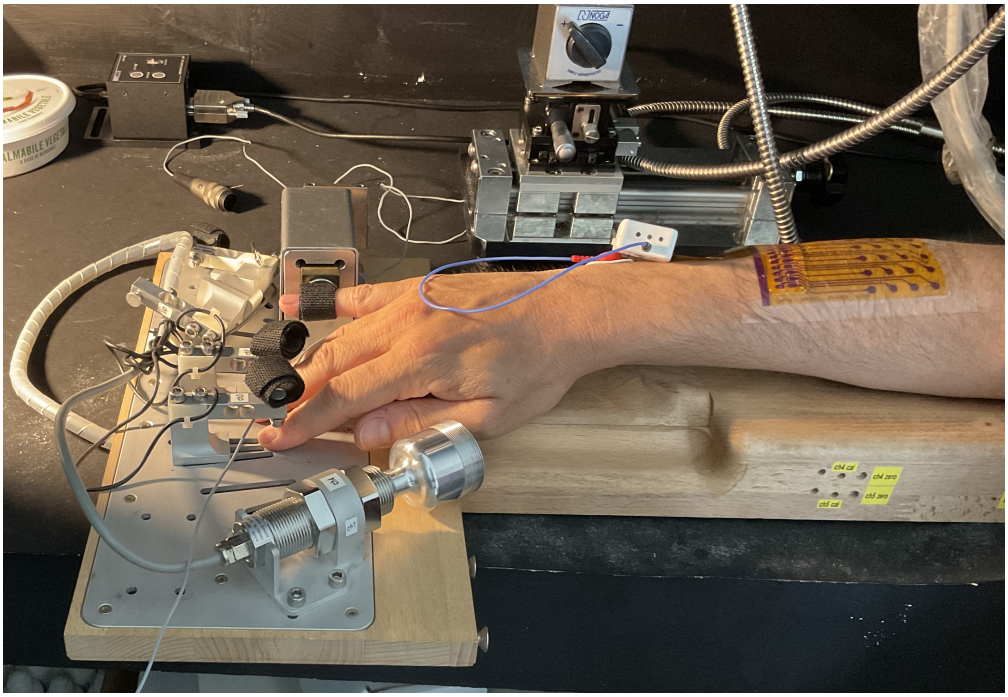

Figure 3.3: Experimental setup featuring a load cell integrated into a custom wooden support, used to continuously record the force applied by the little finger pushing upwards against a resistance.

precise temporal alignment between force measurements and muscle activity. Force measurement data was not saved for the subsequent analysis, but only used as a visual feedback for the exercising subject.

HD-sEMG signals were recorded using a thin-film, ultrasound-transparent electrode array consisting of 32 electrodes arranged in 4 columns and 8 rows. The array was positioned on the forearm over the muscles responsible for finger movements, with the primary target being the EDM muscle, the muscle extending the little finger. Columns (8 electrodes each) were oriented perpendicular to the muscle fibers, while rows (4 electrodes each) were aligned along the fiber direction, allowing each row to capture signals along the fibers (as shown in Figure 3.4).

3.1.5 Preliminary evaluation of electrode array compatibility with photoacoustic imaging

PAI depends on optical absorption and subsequent acoustic wave generation, necessitating an assessment of how electrode materials interact with light to potentially influence signal detection. Prior to subject imaging, a preliminary evaluation was conducted to determine whether the two-dimensional electrode array introduced

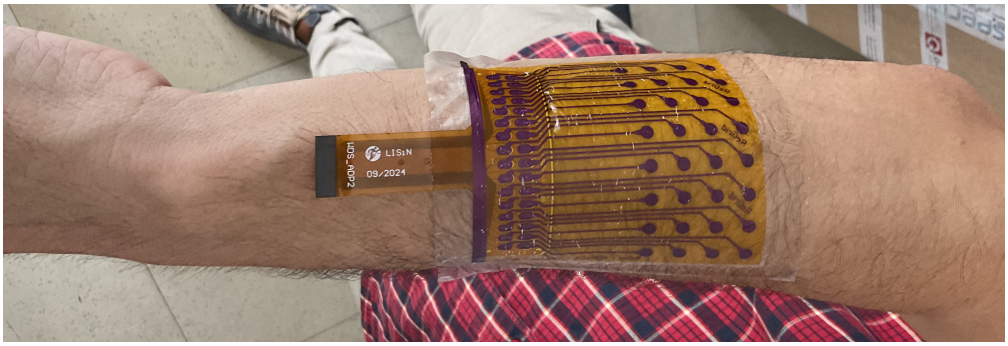

Figure 3.4: Placement of the thin-film, ultrasound-transparent electrode array on the forearm, featuring 32 electrodes in a 8x4 matrix. The array is positioned over the EDM muscle, with columns (8 electrodes each) oriented perpendicular to the muscle fibers and rows (4 electrodes each) aligned along the fiber direction.

signal attenuation, as it forms an additional layer between the skin and transducer. This evaluation utilized a soft tissue-mimicking phantom with carbon pencil leads embedded at varying depths to simulate absorbing structures. The electrode array was placed to cover approximately half of the embedded inserts, enabling a direct comparison of signal intensities between covered and uncovered regions (Figure 3.5 illustrates this setup). The test was repeated on two separate days to verify repeatability. On each day, PA images were acquired at 27 wavelengths from 690 nm to 950 nm in 10 nm increments. For each wavelength, 10 laser pulses were delivered at a 20 Hz repetition rate, yielding 10 frames per wavelength. On the second day, an additional acquisition with 20 pulses per wavelength was performed to assess the impact of extended averaging. Raw data were processed following the pipeline outlined in Section 3.3.1, including delay-and-sum (DAS) beamforming, Hilbert transform-based envelope detection, axial interpolation, decibel-scale conversion, and laser energy normalization prior to frame averaging. Signal attenuation by the electrode array was quantified by defining ROIs over inserts beneath (ROIinside) and outside (ROIoutside) the array, with corresponding background noise ROIs selected nearby. The signal-to-noise ratio (SNR) was computed for each as:

$$\mathrm{SNR}_{\mathrm{dB}} = 20 \cdot \log_{10}\left(\frac{\mu_{\mathrm{signal}}}{\sigma_{\mathrm{noise}}}\right), \tag{3.1}$$

where μ_{signal} is the mean intensity in the signal ROI and σ_{noise} is the standard deviation in the noise ROI. This analysis was applied to all 27 composite images from each acquisition, with comparisons across days, pulse counts (10 vs. 20), and normalization effects. Relevant findings are presented in Chapter 4.

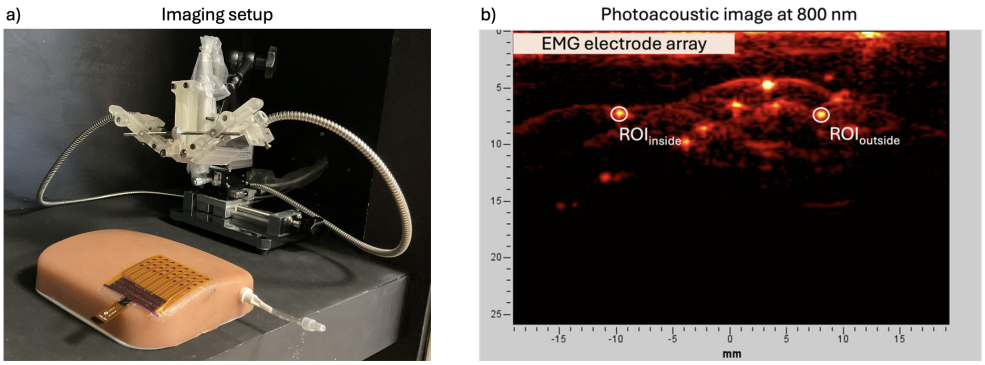

Figure 3.5: (a) Experimental setup for the preliminary phantom evaluation, featuring the soft tissue-mimicking phantom with embedded carbon pencil leads and the electrode array positioned to cover approximately half of the inserts for comparative analysis. (b) Example photoacoustic image at 800 nm, with ROIs defined inside (ROIinside) and outside (ROIoutside) the electrode array coverage, used to quantify signal attenuation via SNR computation.

3.2 Experimental Protocol

3.2.1 Subject positioning and task description

Data acquisition was conducted on two healthy subjects, both over 18 years old, comprising one male and one female. Prior to and following an exercise protocol, each subject was seated on a chair with their right arm resting on a desk, ensuring the wrist remained relaxed and adequately supported. The exercise involved an isometric contraction of the little finger of the right hand, designed to induce muscle fatigue; this was maintained at about 20% of the subject's maximum voluntary contraction for about one minute. To ensure safety, all individuals present in the room wore protective goggles to guard against potential laser exposure. The L11-5v probe was positioned perpendicular to the skin surface over the electrode matrix, secured using standard acoustic coupling gel and an ultrasound gel pad. Before placing the matrix on the forearm, the skin was thoroughly cleaned to optimize contact and signal quality. Simultaneously, photoacoustic and HD-sEMG data were acquired during both rest and fatigue conditions, facilitating a comprehensive analysis of muscle activity.

3.2.2 Data acquisition parameters

Final data, encompassing the complete protocol, were collected across two acquisition sessions on separate days, yielding a total of six complete datasets. Throughout

all experiments, PA and HD-sEMG signals were recorded simultaneously. For PAI, a periodic illumination sequence employed ten different wavelengths, ranging from 700 to 925 nm in 25 nm increments. At each wavelength, the laser delivered short pulses of 5-7 ns duration at a repetition rate of 20 Hz; ten pulses were delivered per wavelength, with a corresponding PA frame captured for each pulse. This resulted in ten consecutive frames per wavelength, which were subsequently averaged to enhance the SNR and produce one representative frame per wavelength. All acquisitions were conducted under both resting and exercise conditions. For subsequent analyses, two wavelength sets were evaluated: the full set of ten wavelengths and a reduced subset of three (750, 800, and 850 nm). The latter was selected to highlight the distinct optical absorption properties of Hb and HbO_2; Hb shows higher absorption around 750 nm, both chromophores exhibit equal absorption at the isosbestic point of 800 nm, and HbO_2 dominates absorption at 850 nm. While HD-sEMG data were collected exclusively during exercise conditions, all raw PA data were stored for offline reconstruction and quantitative processing. Table 3.1 below provides a comprehensive summary of the acquisition parameters, detailing the conditions, wavelength ranges, EMG data collection, and any observed issues across the two subjects over Day 1 and Day 2 experiments.

Subject	Trial	Day	Conditions	Wavelength Range	Number of Wavelengths	EMG / Notes
Male	1	1	Rest + Fatigue	690–910 nm (20 nm step)	11	Fatigue only; 22% data loss EMG
Male	2	1	Rest + Fatigue	700–925 nm (25 nm step)	10	Fatigue only; All ok
Female	1	1	Rest + Fatigue	700–925 nm (25 nm step)	10	Fatigue only; All ok
Female	2	1	Rest + Fatigue	700–925 nm (25 nm step)	10	Fatigue only; 3% data loss EMG
Male	1	2	Rest + Fatigue	700–925 nm (25 nm step)	10	Rest + Fatigue x2; All ok
Male	2	2	Rest + Fatigue	700–925 nm (25 nm step)	10	Rest + Fatigue; 0.5% data loss EMG

Table 3.1: Acquisition parameters for two healthy subjects (one male, one female) across Day 1 and Day 2 experiments. Note that the first trial of the male subject on Day 1 used a different wavelength range (690–910 nm with 20 nm step) compared to the standard 700–925 nm with 25 nm step used in all other trials.

3.3 Data Processing and Analysis

3.3.1 Photoacoustic image reconstruction and processing pipeline

All image processing was performed in MATLAB R2023b (Mathworks, Inc., MA, USA). As previously described, the Verasonics system allows raw data to be saved in .mat files, which were subsequently loaded and analyzed in the software. Each saved file, when loaded in MATLAB, appears as a struct that contains the

acquisition settings, the raw signals received by the transducer, and the transducer specifications. During acquisition, all wavelengths were applied sequentially, with the system automatically cycling through them in a continuous manner. To store the raw data, a buffer containing approximately 700-750 frames was used. For each wavelength, 10 valid samples were collected, resulting in 100 useful frames for a complete cycle of 10 wavelengths. However, the buffer size exceeds this number because of the time required by the laser to switch between wavelengths. Specifically, the laser produced 10 frames with valid image data, followed by an average of ≈ 55 frames without useful information, before resuming with valid data at the next wavelength. This corresponds to $\approx 2.75s$ needed for the laser to complete the wavelength transition at a frame rate of 20 Hz (i.e., $20 \times 2.75 \approx 55$ empty frames). To identify the subset of frames corresponding to the actual useful information in the buffer, an inspection routine was developed. This step was necessary because the relevant frames within the buffer were not fixed a priori; for instance, data acquired at 700 nm could appear in frames 50-59 in one acquisition or 63-72 in another. The inspection procedure therefore allowed us to determine precisely where each wavelength was located within the buffer. An example is shown in Figure 3.6.

A second processing routine was implemented to load both the raw data and the corresponding energy information. The laser energy for each acquisition was recorded using the StarLab software, which saved the data in multiple .txt files. Separate files were generated for each acquisition condition (e.g., rest or fatigue), resulting in a set of energy logs. Each .txt file contained a header with general acquisition information (such as minimum, maximum, and mean energy values, standard deviation, and the total number of pulses), followed by two columns of numerical data. The first column reported timestamps, which clearly reflected the 2.75 s interval corresponding to wavelength switching, while the second column reported the measured pulse energy in Joules. These .txt files were subsequently converted into .mat format for use in MATLAB. For the main image reconstruction stage, the raw datasets, stored as three-dimensional matrices of size $4096 \times 128 \times 700$, corresponding to temporal samples, transducer elements, and frames respectively, were imported into MATLAB. For each selected frame previously identified, the data were organized into two key structures: dataset, containing the reshaped raw signals (10 frames of dimension 1920×128) together with the acquisition parameters, and scan, defining the spatial axes required for image formation. These variables were generated using the get_variables function, which extracts the received channel data and formats it according to the selected acquisition and reconstruction mode (planewave US or PA). At this stage, the raw data were normalized for the laser energy in accordance with the approach described by Diot et al. [33]. Specifically, the single frames (dimension 1920×128) were scaled by multiplying them by the maximum energy value recorded for the given dataset and condition across all

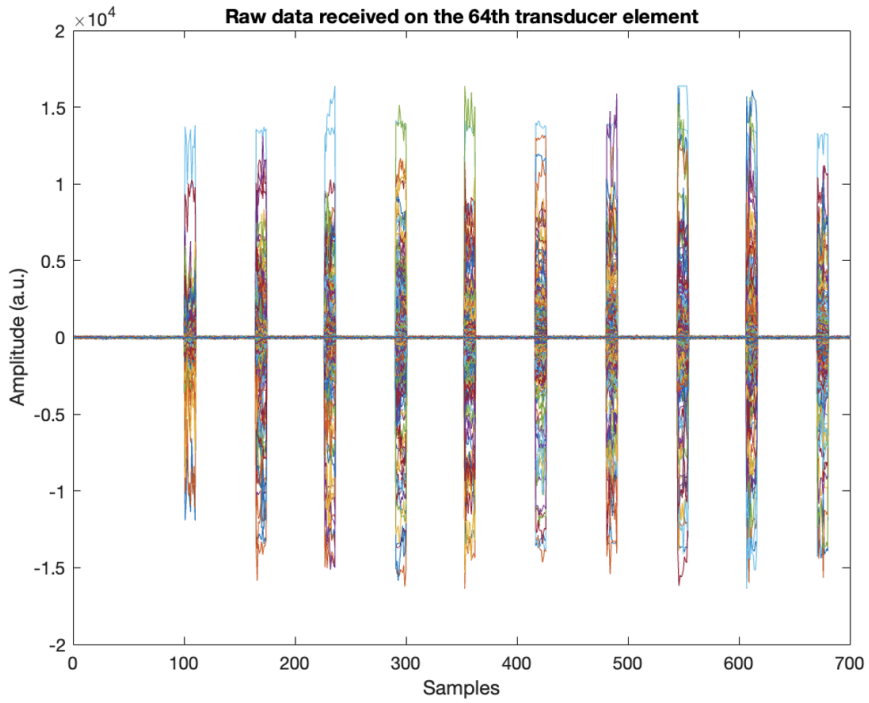

Figure 3.6: Example of raw data received on the 64th transducer element, illustrating the buffer structure with approximately 700-750 frames. The plot shows 10 valid frames per wavelength (highlighted by peaks) within a cycle of 10 wavelengths, followed by approximately 55 empty frames due to the laser wavelength transition, demonstrating the variability in frame positioning requiring the inspection routine.

wavelengths, and dividing it by the energy corresponding to the specific frame under analysis, as follows:

$$data_{norm} = data \cdot \frac{E_{max}}{E_{frame}} \tag{3.2}$$

This normalization was introduced to compensate for fluctuations in laser pulse energy, ensuring that frames acquired with lower pulse energy were appropriately amplified and all data were scaled to a common reference level. Then, image reconstruction was performed using a DAS beamforming algorithm. DAS is a standard reconstruction method in US and PA imaging, where signals received by each transducer element are temporally aligned (delayed) to compensate for differences in propagation paths and then summed, enhancing coherent contributions from the focal point while suppressing incoherent noise (as illustrated in Figure 3.7a). In the implementation of DAS in PA mode, no transmission delay was considered, as the

acoustic waves are generated directly within the tissue following optical absorption; therefore, only the reception delay was accounted for. After DAS reconstruction in PA mode, the processed data were stored in MATLAB structures, organized by acquisition condition and wavelength. Each wavelength field contained ten consecutive frames. For each frame, three image representations were saved:

- `BF`: the raw beamformed data obtained after DAS reconstruction,
- `im_lin`: the image generated after applying the Hilbert transform and envelope detection (i.e., |Hilbert(BF)|),
- `im_dB`: the logarithmic representation after dB conversion.

In addition, spatial information such as the scan axes was stored in the structure. Finally, to obtain a representative image per wavelength, the ten frames were averaged for each image modality. Specifically, the ten lin images were averaged, the ten dB images were averaged, and the ten BF images were averaged for each wavelength (see Figure 3.7b-d for an example mean frame at 800 nm under rest condition). This averaging step not only provided a single representative frame but also improved the SNR by reducing random variability across frames. To compensate for inter-wavelength shifts, primarily observed in lower wavelengths, the averaged images were then aligned using the MATLAB function `imregtform`, with the 925 nm image serving as the fixed reference and all lower wavelength images (700–900 nm) as moving targets, ensuring greater similarity to the overall dataset. The resulting aligned images were used as input for the subsequent spectral unmixing analysis.

3.3.2 ROI selection and metric computation

To evaluate potential differences between rest and fatigue conditions, region-of-interest (ROI) analysis was performed on the averaged images. A representative reference image was first selected, and an ROI was manually delineated in MATLAB using the image acquired at 700 nm. The ROI was positioned in an area exhibiting a strong photoacoustic signal, indicating the presence of absorbing chromophores, though their specific nature was not determined at this stage. The same ROI was then applied across all images within the acquisition, i.e., one averaged image per wavelength. For each ROI, three metrics were extracted: the mean intensity, the maximum intensity, and the 90th percentile of pixel intensities. By applying the identical ROI to both rest and fatigue images, variability due to manual re-selection was minimized, ensuring consistency across conditions. Additionally, a further analysis was conducted. Starting with the image at 700 nm, the manually delineated ROI was used as the basis for applying k-means clustering to identify three distinct classes based on pixel intensity (illustrated in Figure 3.8 for the

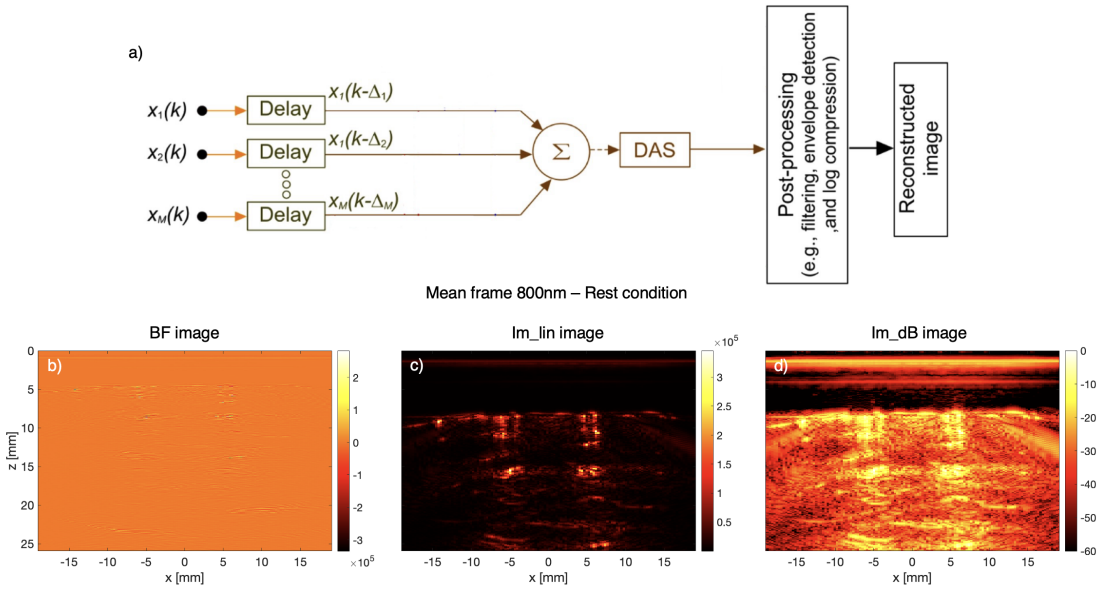

Figure 3.7: (a) Schematic of the DAS beamforming process in PA mode, showing delayed signals $x_i(k - \Delta_i)$ from multiple transducer elements summed to reconstruct the image, followed by post-processing (e.g., envelope detection and log compression). Adapted from [15]. (b-d) Example mean frame at 800 nm under rest condition: (b) BF image (raw beamformed data), (c) Im_lin image (envelope-detected after Hilbert transform), and (d) Im_dB image (logarithmic dB representation), averaged from ten consecutive frames to enhance SNR.

rest condition). This same class subdivision was preserved across all wavelengths, and a mean spectrum was computed for each class over the wavelength range. The resulting mean spectra for the three classes were plotted to visualize spectral variations, with the plots reported in Chapter 4.

3.3.3 Spectral unmixing for oxygenated hemoglobin estimation

As previously introduced, when a laser is used to illuminate a tissue of interest, as in photoacoustic imaging, the chromophores within the tissue absorb the light and emit acoustic waves, which can be detected by an ultrasound transducer. An image acquired at a single wavelength primarily provides structural information, representing the spatial distribution of chromophores that absorbed the light, without distinguishing between different chromophore types. However, by acquiring images at multiple wavelengths, it becomes possible to separate the contributions of individual chromophores. This approach enables the extraction of physiological

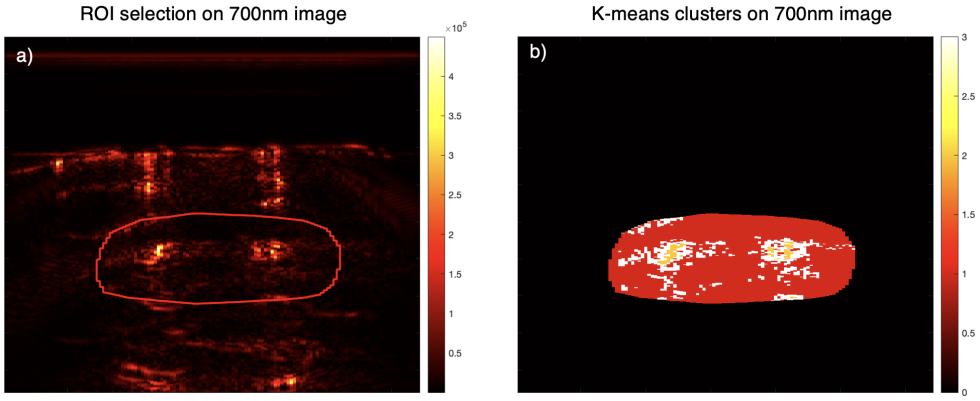

Figure 3.8: Schematic representation of the ROI selection and k-means clustering process applied to the rest condition at 700 nm, showing the manually delineated ROI (a) and the identification of three classes based on pixel intensity (b), with the same subdivision preserved across all wavelengths.

information, such as the relative content of oxygenated hemoglobin versus total hemoglobin in the muscle, which is the focus of the present study. To isolate the contributions of individual chromophores from the multispectral images, a linear spectral unmixing approach was employed. Spectral unmixing is the procedure by which the measured spectrum of a mixed pixel is decomposed into a collection of constituent spectra, or endmembers, and a set of corresponding fractions, or abundances, that indicate the proportion of each endmember present in the pixel. This process commonly adopts a linear mixture model (LMM), which assumes that the measured spectrum at each image location $M(r, \lambda)$ (with r denoting position and λ the optical wavelength) is a linear combination of the spectral signatures $S_i(\lambda)$ of K distinct materials, weighted by their relative abundance or concentration at that specific image location $c_i(r)$:

$$M(r, \lambda) = \sum_{i=1}^{K} S_i(\lambda)\, c_i(r). \tag{3.3}$$

Given knowledge of the spectral signatures $S_i(\lambda)$, the relative concentrations $c_i(r)$ can be estimated by means of linear regression, a method generally referred to as linear unmixing [27]. This was the approach adopted in the present work.

The linear spectral unmixing algorithm employed in this thesis was not developed by the author but provided in Python and executed on Google Colab. The algorithm requires input files in the HDF5 format. For this reason, the averaged images previously obtained in Matlab were reorganized through a dedicated script into multiple HDF5 files and subsequently used as input for the unmixing process.

Each HDF5 file corresponds to a single dataset, containing linear-scale, dB, and BF images. Several unmixing procedures were performed for each dataset. For each image modality, two separate unmixings were carried out: one using the full spectral range (700-925 nm, 25 nm steps), and one restricted to three wavelengths (750, 800, and 850 nm). The rationale for this reduced set is that Hb exhibits higher absorption near 750 nm, both chromophores share the same absorption at 800 nm (isosbestic point), and HbO_2 becomes the dominant absorber around 850 nm. The molar extinction coefficients of hemoglobin in water, reported by Scott Prahl [34], were used as reference spectra. Specifically, both HbO_2 and Hb spectra were available in the range 250–1000 nm with a 2 nm step size, expressed in cm^{-1}/M. Since the acquisition wavelengths were sampled with 25 nm intervals, the spectral data required interpolation to match the measurement grid. This was performed in MATLAB using the `interp1` function with the spline interpolation method, in order to generate values at the required wavelengths. These interpolated spectra were then used as the reference signatures in the linear unmixing model.

Before applying spectral unmixing, several preprocessing strategies were explored to improve the stability of the decomposition. These included pixel-wise min-max scaling across wavelengths, global maximum normalization, image cropping, block-wise spatial averaging, and intensity thresholding. In particular, min-max scaling normalized each wavelength-specific image to its local dynamic range, whereas global maximum normalization scaled all frames by the maximum intensity observed across the entire dataset. Cropping was applied to remove background regions outside the imaging field of interest, while block-wise averaging (MATLAB `blockproc`, 3×3 window) was tested to reduce the number of pixels and mitigate local variability. Intensity thresholding was also investigated by applying three different cutoff levels to suppress low-intensity values likely dominated by noise. However, except for the intensity thresholding, none of these preprocessing steps substantially improved the unmixing performance. Therefore, the analysis presented in this thesis is based solely on the laser energy normalization previously described.

Spectral unmixing was then performed on a pixel-wise basis using a constrained linear least-squares solver. The model matrix contained the interpolated reference spectra of HbO_2 and Hb, and the measured spectrum at each pixel was fitted as a non-negative linear combination of these signatures. The fitting was implemented through the `lsq_linear` function in Python, with bounds enforcing non-negative concentrations for both HbO_2 and Hb. From the fitted coefficients, total hemoglobin ($HbT = HbO_2 + Hb$) was computed, and the oxygen saturation (sO_2) was expressed as the ratio HbO_2/HbT. A check was included to avoid division by zero in pixels with negligible signal. The resulting maps were subsequently restricted to the selected ROI, both with and without the application of intensity thresholds.

Once the unmixing results were obtained, the resulting sO_2 maps acquired under both resting and fatigued conditions were further analyzed. A k-means clustering

algorithm was applied to the unmixed images to segment the tissue into three clusters based on oxygen saturation levels, corresponding to low, medium, and high oxygenation. After identifying the three clusters, the resulting cluster map was stored and subsequently applied to the original PA images. For each cluster, the mean spectrum and standard deviation across wavelengths were computed. This procedure enabled the generation of spectral curves that describe the behavior of the three oxygenation clusters as a function of wavelength. These curves, together with the centroid values obtained for each cluster, are presented in Chapter 4.

3.3.4 HD-sEMG signal processing and feature extraction

Raw EMG signals were first reconstructed from the acquired data levels and converted from ADC units to volts referred to input (V^{RTI}). For each channel, the percentage of data loss was then computed as a quality check, with deviations from zero observed in some acquisitions, as reported in Table 3.1. To correct for baseline drift, the mean value was subtracted from each channel before further processing. Subsequently, the monopolar signals were band-pass filtered between 20–400 Hz using a fourth-order Butterworth filter, in order to isolate the relevant EMG frequency components. Since line noise at 50 Hz was visible in the power spectral densities (PSDs) of certain channels, a fourth-order Butterworth notch filter centered at 50 Hz with a narrow stopband (48–52 Hz) was applied. This operation was performed prior to computing the single differential (SD) signals, thereby reducing power line interference while preserving the physiological content of the EMG. Although higher harmonics at multiples of 50 Hz were also detected in the PSDs, these were not removed, as their presence was not expected to affect the outcomes of this work. After these preprocessing steps, SD signals were derived from the monopolar signals to improve spatial selectivity and suppress common-mode noise. Differences were computed along the columns of the electrode grid, i.e., aligned with the muscle fibers, resulting in an 8×3 SD channel configuration. This orientation ensured that the obtained SD signals faithfully reflected the physiological alignment of the EDM muscle.

The aim of the analysis was to evaluate if and how myoelectric manifestations of muscle fatigue are distributed across the electrode grid. To do so, both monopolar and SD signals were considered in the subsequent analyses. The rationale for including both modalities is technical. Monopolar recordings, obtained by referencing each electrode of the HD-EMG array to a reference electrode placed on the wrist, provide a direct representation of the acquired signals but are more prone to noise contamination and cross-talk from adjacent muscles. In contrast, SD recordings, obtained as the difference between neighboring electrodes along the muscle fibers, effectively attenuate common-mode disturbances and enhance the selectivity toward MUAPs. For this reason, the analysis was conducted in parallel

on both monopolar and SD signals: monopolar signals were used to illustrate the quality and origin of the acquired data, while SD signals were employed to obtain cleaner, spatially resolved maps of muscle activation. The combination of both perspectives ensured a more comprehensive assessment of the spatial distribution of myoelectric manifestations of fatigue across the electrode grid.

To quantitatively assess changes in muscle activation during sustained contraction, the RMS of the EMG signals was computed on non-overlapping 0.5 s epochs for all channels. This procedure yielded approximately 100 RMS values per channel. From these, three representative periods were selected: the onset, the middle, and the final phase of the contraction. The onset and middle phases were defined as the first and central epochs, respectively, while the final phase was identified as the portion exhibiting the highest RMS value (indicative of peak activation during fatigue), as subsequent epochs typically showed a decrease in RMS, likely due to the subject no longer maintaining the contraction. For each phase, the RMS values were spatially mapped, thus generating three activation maps per configuration. These maps allowed for the visualization of changes in muscle activation over time, highlighting electrodes under which higher RMS values were observed, and providing insights into the localization and evolution of the activation pattern during the task.

After generating the spatial RMS maps, a further analysis was performed to investigate muscle fatigue in the most active region of the electrode grid. This analysis was conducted for both monopolar and SD signals, consistent with all preceding procedures. The most active areas were identified from the previously obtained RMS maps, and only the channels exhibiting the highest activity were selected, as the objective was to assess fatigue in the region predominantly contributing to muscle contraction. For each selected channel, RMS and MNF values were computed on consecutive 0.5 s epochs, yielding time series that were then fitted with a first-order polynomial in the least-squares sense, resulting in an equation of the form $y = px + q$. The slope coefficient (p) was extracted for each channel, and these slopes were averaged across the selected electrodes to obtain mean slope values for both RMS and MNF. To verify the fitting process, the superimposed polynomial fits were plotted alongside the corresponding RMS and MNF time series for the selected electrodes. Figure 3.9 below summarizes the HD-sEMG processing steps.

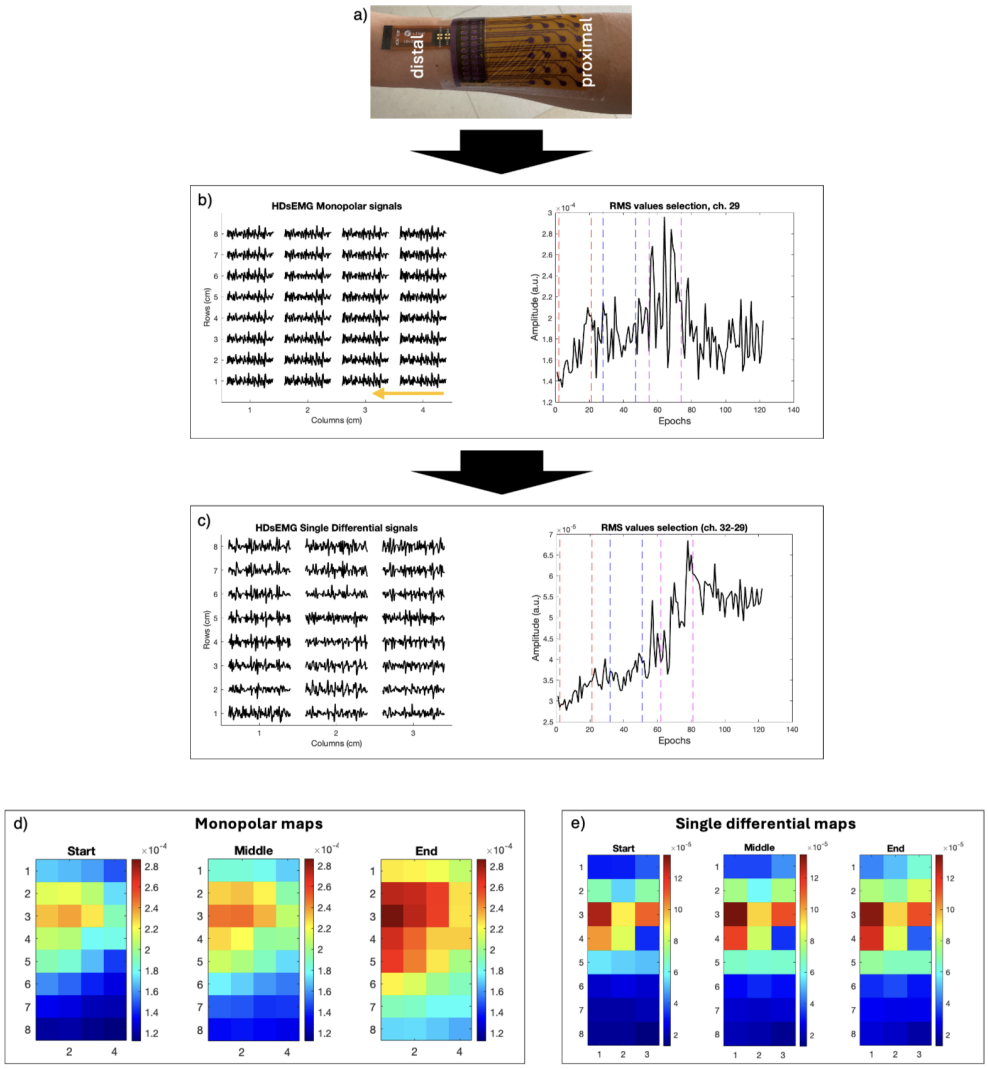

Figure 3.9: Illustration of HD-sEMG signal processing pipeline for the first acquisition (male subject, Day 1). (a) Electrode array placement on the forearm. (b) Monopolar signals (left) and RMS value selection for channel 29 (right). (c) Single differential signals (left) and RMS for channels 29–32 (right). (d) Interpolated monopolar RMS maps for start, middle, and end phases. (e) Interpolated single differential RMS maps for start, middle, and end phases. Color scale: RMS amplitude (arbitrary units); orientation: lateral (up), medial (down), distal (left), proximal (right).

Chapter 4

Results

4.1 Results of the preliminary evaluation of electrode array compatibility

The preliminary phantom evaluation demonstrated the electrode array's compatibility with PAI, revealing consistent but moderate signal attenuation (mean SNR difference of 5.3 ± 0.2 dB between $\mathrm{ROI}_{\mathrm{inside}}$ and $\mathrm{ROI}_{\mathrm{outside}}$ across 27 wavelengths for the 10-frame acquisitions on Days 1 and 2, corresponding to a relative difference of 18.8%). Repeatability between the two acquisition days was evident, with normalized SNR profiles showing a mean variation of 7.6% relative to Day 1 values. Increasing the number of averaged frames from 10 to 20 on Day 1 yielded a modest SNR improvement of 0.2% on average (0.8% inside, −0.4% outside), suggesting limited additional benefit from extended averaging in this setup. ROIs were selected as described in Section 3.1.5 (see Figure 3.5 for an example placement). These findings are detailed in Figure 4.1, showing unnormalized and normalized (panels a, b) SNR comparisons across days, along with the effect of frame averaging on Day 1 (panel c). Quantitative summaries, including mean differences, are provided in Table 4.1.

Acquisition	Frames	Mean SNR outside (dB)	Mean SNR inside (dB)	Max SNR outside (dB)	Max SNR inside (dB)	Min SNR outside (dB)	Min SNR inside (dB)
Day 1	10	27.98 ± 3.676	33.1 ± 3.868	39.22	45.39	23.98	27.66
Day 1	20	27.86 ± 3.622	33.35 ± 4.132	38.43	46.5	23.83	27.49
Day 2	10	30.11 ± 3.353	35.64 ± 3.935	41.42	50.8	26.1	30.44

Table 4.1: Mean SNR values measured inside and outside the electrode array across different acquisition conditions and frame averaging levels.

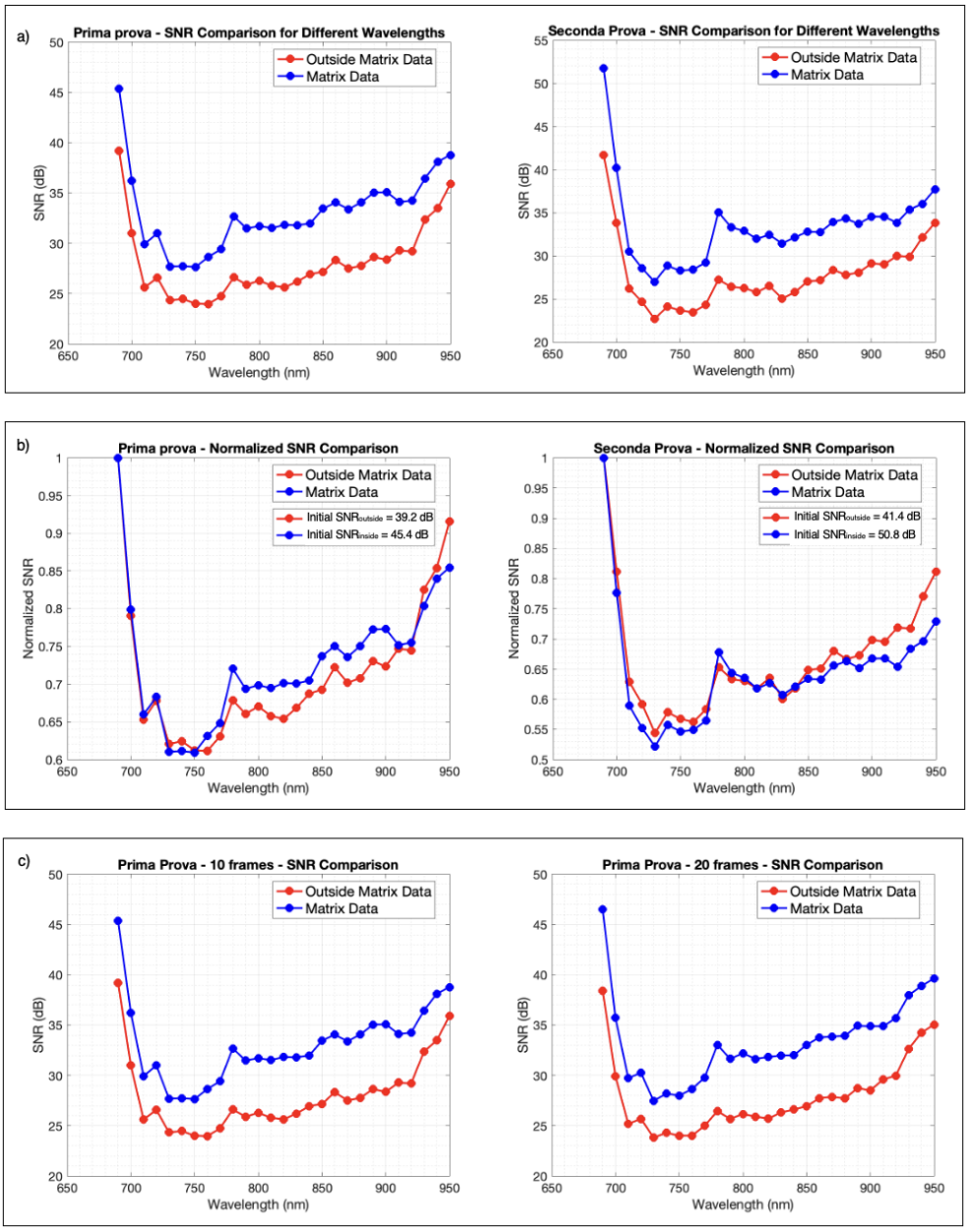

Figure 4.1: SNR analysis from the preliminary phantom evaluation across 27 wavelengths (690-950 nm). (a) Unnormalized SNR for Day 1 (left) and Day 2 (right) acquisitions, comparing $\mathrm{ROI}_{\mathrm{outside}}$ (red) and $\mathrm{ROI}_{\mathrm{inside}}$ (blue). (b) Normalized SNR (to initial value) for Day 1 and Day 2, with initial SNR indicated. (c) SNR from 10-frame and 20-frame averaging on Day 1.

4.2 Photoacoustic Imaging results

4.2.1 Full-Field Spectral Unmixing (Rest vs. Fatigue)

Full-field spectral unmixing was applied to the averaged photoacoustic images across all six acquisitions, estimating distributions of oxygenated (HbO_2) and deoxygenated hemoglobin (Hb) for rest and fatigue conditions. For a representative acquisition (Acquisition 1: Day 1, female subject), unmixing using the reduced subset of three wavelengths (750, 800, 850 nm) produced images with localized oxygenation fractions in superficial vascular structures during rest, transitioning to more diffuse patterns in fatigue (Figure 4.2, left column). Extending to the full set of 10 wavelengths (700-925 nm) yielded comparable spatial distributions but with enhanced contrast in deeper regions, particularly for oxygenation fractions in fatigue (Figure 4.2, right column). Similar trends in chromophore localization were observed across the remaining acquisitions.

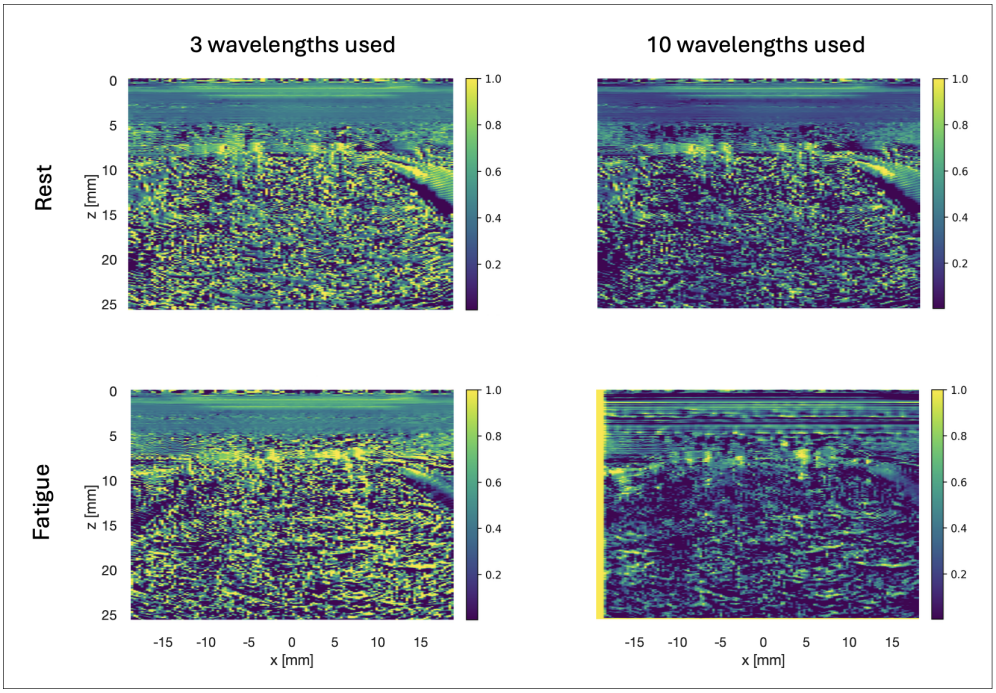

Figure 4.2: Full-field spectral unmixing results for a representative acquisition (Acquisition 1: Day 1, female subject), comparing the reduced 3-wavelength subset (750, 800, 850 nm; left column) to the full 10-wavelength set (700-925 nm; right column). Images depict the oxygenation fraction $[\frac{HbO_2}{HbO_2+Hb}]$, normalized to 0-1. Top row: Rest condition, showing primarily superficial vascular signals. Bottom row: Fatigue condition, exhibiting more extended patterns.

4.2.2 ROI-Limited Spectral Unmixing

ROI-limited spectral unmixing was performed on the averaged PA images from all six acquisitions, focusing on the manually delineated region over the EDM that exhibited stronger PA signal (as defined in Section 3.3.2). For the representative first acquisition of the male subject on Day 2, unmixing using the full 10-wavelength set (700–925 nm in 25 nm steps) was applied to cropped versions of the original images, followed by masking to confine the analysis to the ROI (Figure 4.3a). This approach isolated signals to the central muscle region, reducing peripheral artifacts in both rest and fatigue conditions. K-means clustering ($k = 3$) applied to the 700 nm PA ROI image identified distinct pixel groups based on intensity in both rest and fatigue, with the red-masked areas corresponding to blue clusters (Cluster 1), yellow-clustered areas to red (Cluster 2), and white areas to yellow (Cluster 3) (Figure 4.3b, left). The mean spectra per cluster, computed across all wavelengths with standard deviation, showed varying absorption profiles, with Cluster 2 exhibiting higher amplitudes at shorter wavelengths while Cluster 1 and Cluster 3 remained relatively constant and lower in intensity. Comparable ROI-limited patterns and clustering results were observed in the other acquisitions. In addition to intensity-based clustering, the unmixed sO_2 maps obtained from the same acquisitions were further analyzed using k-means clustering (k = 3) to group pixels according to their oxygenation levels. The resulting cluster maps were then used to extract the mean spectral response of each cluster from the original PA images across all wavelengths. This enabled a direct comparison between regions characterized by low, intermediate, and high oxygenation. The spectral curves, along with their standard deviations, revealed distinct absorption trends associated with different oxygenation levels, further highlighting functional differences within the muscle tissue (Figure 4.4). Centroid values corresponding to each cluster for both rest and fatigue conditions are reported in Table 4.2. These results complement the intensity-based analysis described previously, providing additional physiological insight.

4.2.3 Thresholded Spectral Unmixing

Thresholded spectral unmixing was applied to the averaged PA images from all six acquisitions, using three cutoff levels (8000, 10000, and 15000 arbitrary units of PA signal amplitude) to suppress low-intensity pixels by eliminating everything below those values prior to unmixing, as described in Section 3.3.3. For the two acquisitions of the male subject on Day 2, full-field results without ROI showed progressively sparser SO_2 distributions with increasing threshold levels in both rest and fatigue conditions (Figure 4.5, top and middle rows). When limited to the ROI, signals concentrated in central vascular areas at all thresholds, with rest exhibiting more punctate patterns and fatigue displaying extended coverage compared to

Subject/Day	**Acquisition**	**Cluster 1 (Low)**	**Cluster 2 (Mid)**	**Cluster 3 (High)**
Male/Day 1	1st Rest	0.0857	0.4218	0.7378
Male/Day 1	1st Fatigue	0.0101	0.2942	0.6369
Male/Day 1	2nd Rest	0.0236	0.3227	0.6703
Male/Day 1	2nd Fatigue	0.0339	0.3196	0.6285
Female/Day 1	1st Rest	0.0429	0.3648	0.7165
Female/Day 1	1st Fatigue	0.0342	0.3180	0.6454
Female/Day 1	2nd Rest	0.0411	0.3095	0.5946
Female/Day 1	2nd Fatigue	0.0380	0.3422	0.6575
Male/Day 2	1st Rest	0.0598	0.3625	0.6356
Male/Day 2	1st Fatigue	0.0907	0.4280	0.7460
Male/Day 2	2nd Rest	0.0782	0.3494	0.6270
Male/Day 2	2nd Fatigue	0.0438	0.3364	0.6596

Table 4.2: Cluster centroid values obtained from k-means segmentation of the ROI in rest and fatigue conditions, across all acquisitions. Cluster 1 represents low sO_2, Cluster 2 mid sO_2, and Cluster 3 high sO_2.

the full-field views (Figure 4.5, bottom row). Similar threshold effects were noted across the other acquisitions.

4.2.4 Comparative analysis across acquisitions and conditions

ROI-limited spectral unmixing metrics across the six acquisitions showed varying mean SO_2 fractions within the delineated region, with values ranging from 0.099 to 0.419 (Table 4.3). For the male subject on Day 1, mean SO_2 decreased from 0.410 in rest to 0.099 in fatigue for the first acquisition, while the second showed an increase from 0.193 to 0.232. The female subject on Day 1 exhibited modest increases (0.228 to 0.271 for the first; 0.253 to 0.261 for the second). On Day 2, the male subject's first acquisition displayed a rise from 0.330 to 0.419, whereas the second showed a slight decrease from 0.313 to 0.263. These values, normalized to a maximum of 1 (fully oxygenated hemoglobin), highlight condition-specific shifts in oxygenation within the ROI.

Subject/Day	**Acquisition**	**Rest Mean SO_2**	**Fatigue Mean SO_2**
Male/Day 1	1st	0.410	0.099
Male/Day 1	2nd	0.193	0.232
Female/Day 1	1st	0.228	0.271
Female/Day 1	2nd	0.253	0.261
Male/Day 2	1st	0.330	0.419
Male/Day 2	2nd	0.313	0.263

Table 4.3: ROI-limited mean SO_2 values in rest and fatigue conditions across the six acquisitions.

4.3 HD-sEMG Results

4.3.1 Spatial activation maps (RMS)

Spatial activation maps were generated from RMS values computed on 0.5 s epochs for the monopolar and SD configurations across all channels in the six acquisitions, with phases selected as the onset, middle, and final (highest RMS epoch) of contraction per Section 3.3.4. For the first acquisition of the male subject on Day 1, monopolar maps displayed RMS hotspots ($> 2.8 \times 10^{-4}$ V) concentrated in the central-medial region during the onset phase, maintaining a stable central distribution through the middle phase, and remaining similarly centered in the final

phase (Figure 4.6, top row). SD maps showed comparable central stability, with peak RMS values (up to 9×10^{-5} arbitrary units) in the medial-central electrodes across all phases, exhibiting a more uniform circular pattern without notable shifts (Figure 4.6, bottom row). Interpolation via spline method was applied for visualization smoothness. Similar stable activation patterns were observed in the remaining acquisitions.

4.3.2 Fatigue indicators (slopes for RMS and MNF)

Fatigue indicators were derived from linear fits to RMS and MNF time series computed on 0.5 s epochs in the most active electrode regions, as identified from spatial RMS maps per Section 3.3.4, for both monopolar and SD configurations across all six acquisitions. For a representative first acquisition of the female subject on Day 1 (monopolar signals, channels 13–24), RMS slopes across the active channels ranged from 1.56×10^{-6} to 2.41×10^{-6} V/s, with a mean slope of 1.94×10^{-6} V/s, showing gradual increases over the 30 s contraction (Figure 4.7, top row). MNF slopes in the same region varied from -0.47 to -0.35 Hz/s, with a mean of -0.42 Hz/s, exhibiting consistent downward trends with minor fluctuations (Figure 4.7, bottom row). Mean slopes for all acquisitions and configurations are summarized in Table 4.4, revealing channel-specific variations within the active regions.

Acquisition	**Configuration**	**Active Channels**	**Mean RMS Slope (V/s)**	**Mean MNF Slope (Hz/s)**
Male Day 1, 1st	Monopolar	13–24	-6.82×10^{-7}	-0.212
Male Day 1, 1st	Single Diff.	17–28	-1.32×10^{-7}	-0.0603
Male Day 1, 2nd	Monopolar	13–24	4.80×10^{-7}	-0.409
Male Day 1, 2nd	Single Diff.	17–28	7.26×10^{-8}	-0.619
Female Day 1, 1st	Monopolar	13–28	1.94×10^{-6}	-0.417
Female Day 1, 1st	Single Diff.	13–28	3.88×10^{-7}	-0.668
Female Day 1, 2nd	Monopolar	13–28	6.10×10^{-7}	-0.196
Female Day 1, 2nd	Single Diff.	13,17,21–28	3.40×10^{-9}	-0.654
Male Day 2, 1st	Monopolar	25–32	-7.07×10^{-7}	-0.382
Male Day 2, 1st	Single Diff.	25–32	-3.28×10^{-7}	-0.737
Male Day 2, 2nd	Monopolar	25–32	1.64×10^{-6}	-0.811
Male Day 2, 2nd	Single Diff.	25–32	5.72×10^{-7}	-1.111
Male Day 2, 3rd	Monopolar	25–32	-2.27×10^{-7}	-0.215
Male Day 2, 3rd	Single Diff.	25–32	4.33×10^{-9}	-0.670

Table 4.4: Mean RMS and MNF slope values computed in the most active channels for each acquisition and configuration across the six experimental sessions.

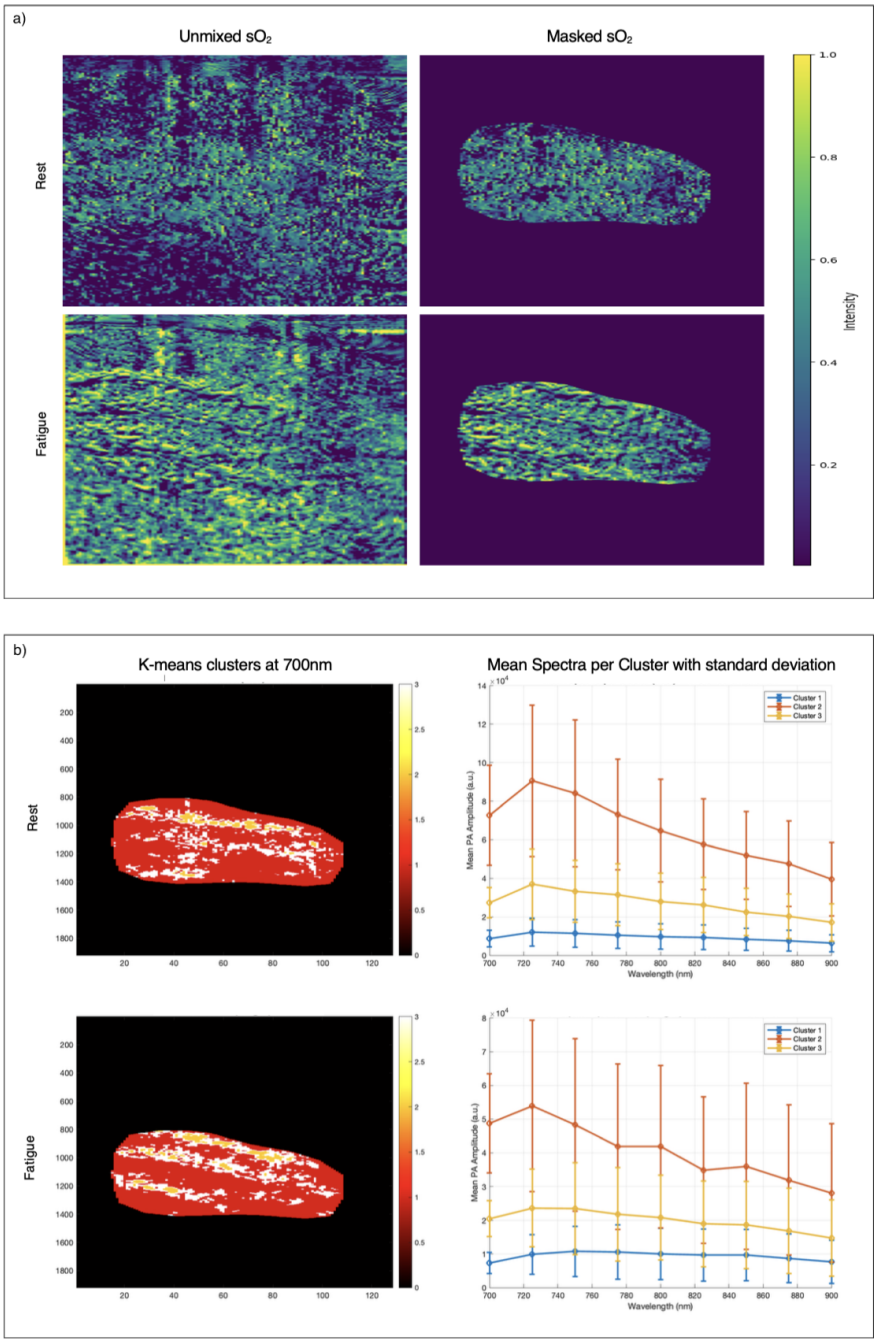

Figure 4.3: ROI-limited spectral unmixing results for the first acquisition of the male subject on Day 2, using 10 wavelengths (700–925 nm in 25 nm steps) on cropped images masked to the ROI. (a) Oxygenation fraction (SO_2) distributions: unmixed rest (top left), masked rest (top right), unmixed fatigue (bottom left), and masked fatigue (bottom right), showing confined vascular signals in rest and broader extension in fatigue. (b) K-means clustering ($k = 3$) on the 700 nm ROI image for rest (left) and fatigue (right), with color-coded clusters (blue: Cluster 1 [red in mask], red: Cluster 2 [yellow in cluster], yellow: Cluster 3 [white in cluster]); accompanying mean spectra per cluster across wavelengths, with standard deviation.

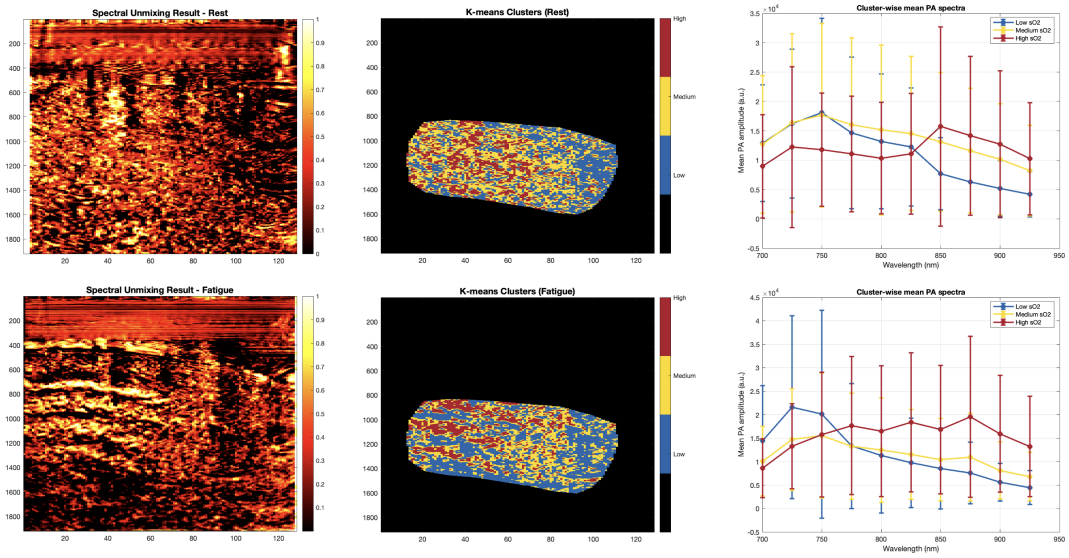

Figure 4.4: Representative results of cluster-based spectral analysis performed on the unmixed sO_2 map of a male subject (Day 2 acquisition), in rest (top row) and fatigue (bottom row) conditions. Left: Unmixed sO_2 maps obtained through spectral unmixing of the averaged PA images within the ROI. Center: K-means clustering (k = 3) applied to the sO_2 maps, segmenting the tissue into three clusters based on oxygenation levels: low (blue), medium (yellow), and high (red). Right: Cluster-wise mean PA spectra with standard deviation, computed from the original PA images across wavelengths (700-925 nm, 25 nm steps). Distinct spectral trends can be observed across clusters, reflecting physiological differences between oxygenation levels and experimental conditions.

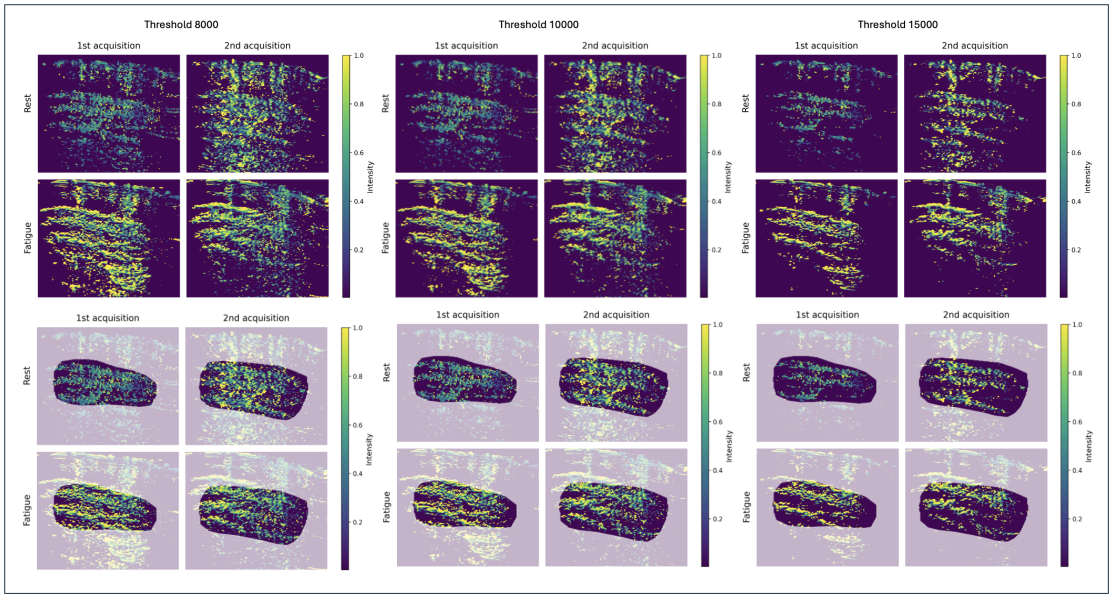

Figure 4.5: Thresholded spectral unmixing results for the two acquisitions of the male subject on Day 2, using 10 wavelengths (700–925 nm in 25 nm steps) and cutoff levels of 8000 (left column), 10000 (middle column), and 15000 (right column) arbitrary PA amplitude units. Top row: Full-field rest condition for 1^{st} and 2^{nd} acquisitions. Middle row: Full-field fatigue condition for 1^{st} and 2^{nd} acquisitions. Bottom rows: ROI-limited versions for rest and fatigue. Color scale: normalized SO_2 (0–1).

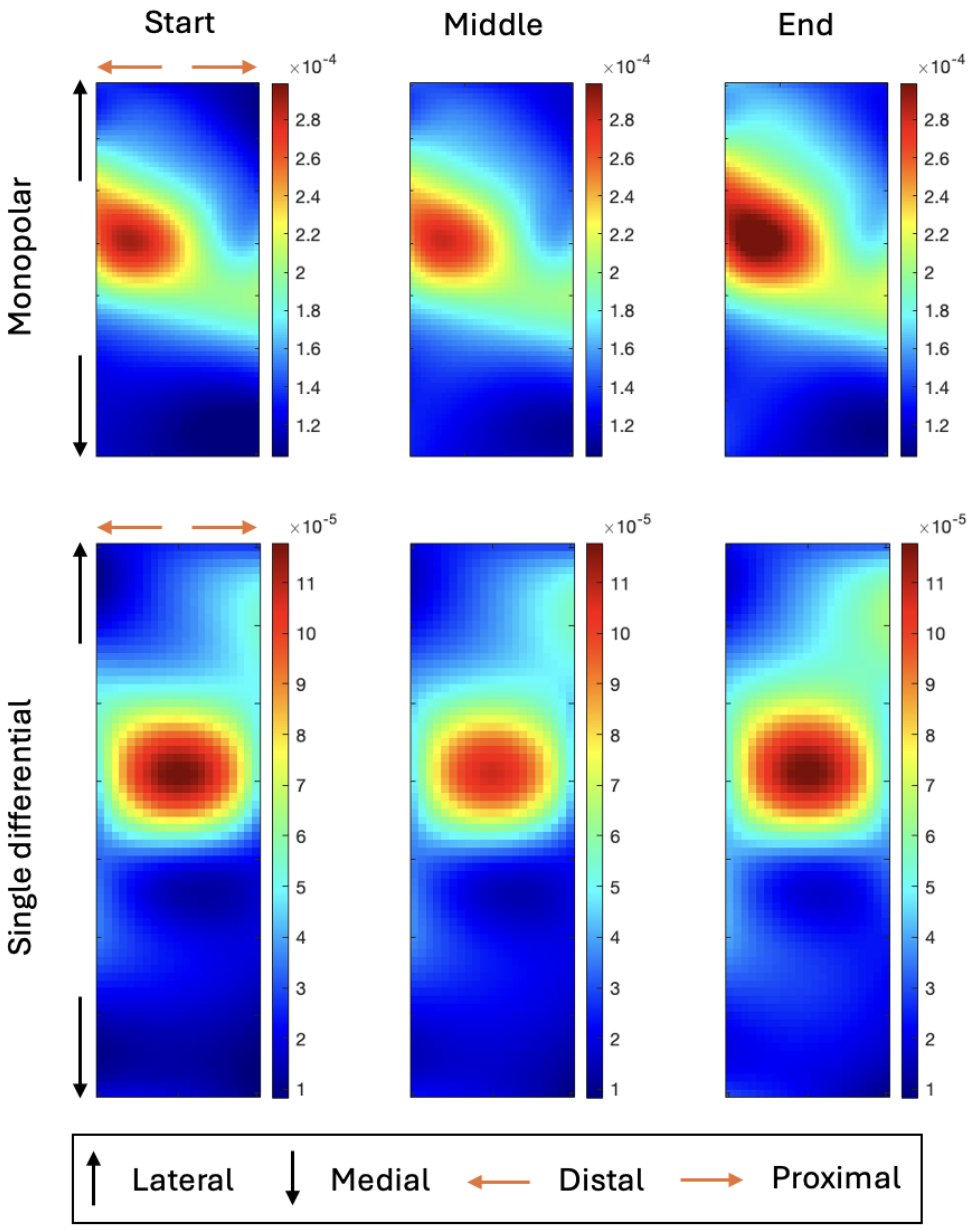

Figure 4.6: Interpolated spatial RMS activation maps for the first acquisition of the male subject on Day 1, showing onset (left column), middle (center column), and final (right column) phases. Top row: Monopolar configuration, with stable central-medial hotspots. Bottom row: SD configuration, displaying centered circular patterns. Grid: 8 rows × 4 columns for monopolar configuration and 8 rows × 3 columns for SD configuration (spline-interpolated for smoothness).

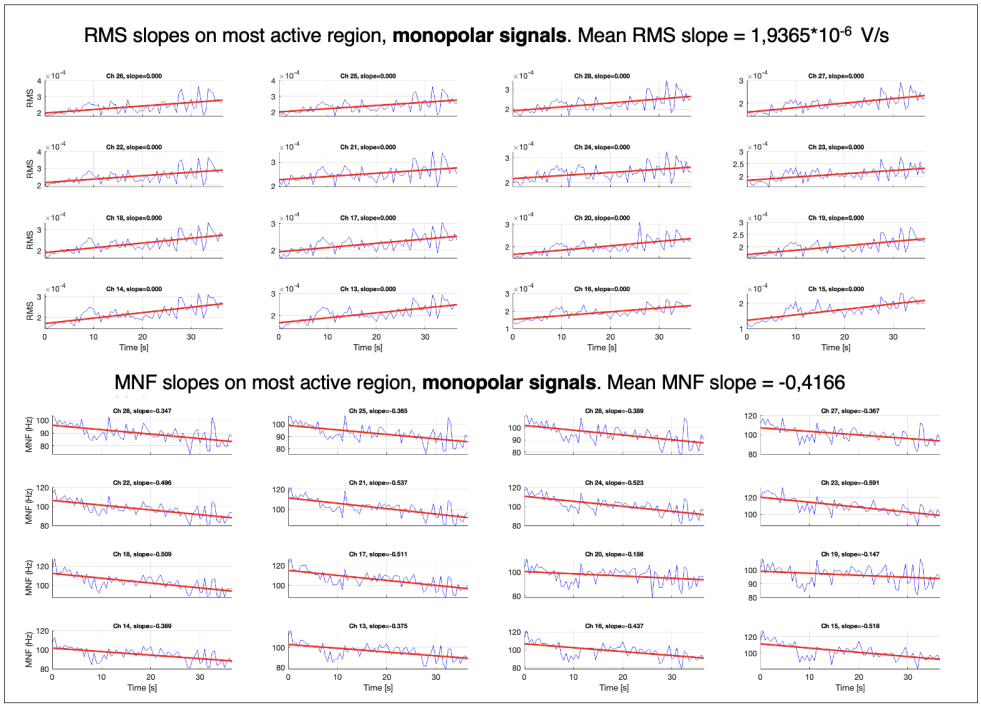

Figure 4.7: Linear slope fits for RMS and MNF time series in the most active region (channels 13–24) for the first acquisition of the female subject on Day 1, monopolar configuration. Top row: RMS slopes for individual channels (blue lines) with fits (red), mean slope = 1.94×10^{-6} V/s. Bottom row: MNF slopes for individual channels (blue) with fits (red), mean slope = -0.42 Hz/s. Time axis: 0–30 s; y-axis: RMS ($\times 10^4$ V) or MNF (Hz).

Chapter 5

Discussion

The preliminary phantom evaluation yielded unexpected yet insightful results regarding the electrode array's interaction with PA signals. Contrary to the initial hypothesis that the matrix might attenuate the detected acoustic waves due to its positioning as an additional layer between the tissue-mimicking phantom and the transducer, unnormalized SNR values were significantly higher in regions beneath the array across all tested wavelengths (690-950 nm). Between the two trials conducted on separate days, the second acquisition exhibited slightly elevated SNR levels compared to the first. This difference can be attributed to a substantially lower standard deviation in the noise ROI for the second trial (an order of magnitude below that of the first), while signal means remained comparable in magnitude, suggesting reduced background noise overall. These observations may arise from a combination of physical mechanisms, including improved acoustic coupling at the electrode-phantom interface, reflections and wave redirection induced by the array's geometry and acoustic impedance, localized alterations in optical fluence, and potential shielding of acoustic/electrical background noise. Such effects align with existing literature on acoustic impedance matching and metallic interfaces in US/PA systems [35, 36]. To disentangle these contributions, future experiments could incorporate controls such as additional coupling gel or spectral analysis of the signals.

Turning to the PAI analysis, the reconstructed images clearly delineated regions of elevated optical absorption, consistent with the presence of chromophores in the EDM muscle. In the ROI-based cluster analysis, consistent patterns emerged across all acquisitions: the background cluster exhibited the lowest mean intensity, remaining stable across wavelengths, while the intermediate cluster showed minimal variation; in contrast, the cluster corresponding to high-PA-signal zones displayed elevated amplitudes at shorter wavelengths, progressively declining toward longer ones. This spectral trend was evident in both rest and fatigue conditions, potentially reflecting a predominance of Hb (with peak absorption near 750 nm) over HbO_2

(peaking near 850 nm), though the analysis at this stage did not yet distinguish specific chromophores and may simply indicate broader differential absorption by tissue constituents at lower wavelengths. When applying k-means clustering to the unmixed images, a complementary and more physiologically meaningful trend emerged: the cluster associated with low oxygenation levels showed higher PA amplitudes at lower wavelengths, whereas the high-oxygenation cluster exhibited increased responses at longer wavelengths. This behavior aligns well with the expected absorption characteristics of Hb and HbO_2, further supporting the interpretation of the spectral patterns observed in the non-unmixed data.

Spectral unmixing results, however, proved challenging to interpret, often yielding ambiguous distributions. Physiologically, the EDM at rest was anticipated to exhibit relatively high oxygenation fractions (sO_2), with uniform ROI coverage; during isometric contraction of the little finger, increased oxygen consumption and potential capillary compression were expected to reduce local blood flow, leading to decreased sO_2 and possible spatial gradients from central to peripheral muscle regions. In contrast, the acquired data revealed unexpectedly low mean sO_2 values within the ROI even at rest (approximately 0.2), accompanied by slight increases during fatigue, a reversal of the predicted desaturation. Notably, the second rest acquisition for the male subject on Day 2 showed higher oxygenation than the first, possibly attributable to post-contraction revascularization enhancing perfusion. These discrepancies suggest influences from methodological or instrumental factors, such as the limited spectral resolution of the linear unmixing algorithm, the linear ultrasound transducer's field of view, or motion artifacts during contraction. Validation against alternative oxygenation measurement techniques is essential to refine interpretations of contraction-induced changes.

The reviewed literature on PAI primarily addresses reperfusion dynamics post-exercise [18, 22] or during/after cuff occlusion [20, 21, 24]. Occlusion studies indicate that venous blockade maintains arterial inflow, elevating both HbO_2 and Hb signals due to impeded outflow, with gradual baseline recovery upon release; arterial occlusion, conversely, diminishes incoming oxygenated blood, reducing both species (particularly Hb), followed by rebound increases post-release. Post-exercise investigations similarly document muscle reperfusion as a hallmark of recovery. The work most akin to the present study is that of Karlas et al. [19], who examined brachioradialis perfusion before, during, and after isometric contraction using multispectral optoacoustic tomography at discrete wavelengths (750 nm mean signal was considered as Hb, 800 nm as total blood volume, 850 nm as HbO_2), without spectral unmixing. Their temporal profiles revealed signal decreases during contraction and subsequent increases afterward, mirroring expected hemodynamic shifts.

Regarding HD-sEMG, the initial hypothesis of spatially localized muscle activation, stemming from the selective contraction of a discrete muscle, was unequivocally

supported, with higher RMS activity confined to specific electrodes across all acquisitions. Furthermore, the most active zones demonstrated fatigue signatures, as evidenced by consistently negative MNF slopes, affirming established neuromuscular physiology where spectral compression accompanies sustained effort.

Despite these advances, several limitations warrant acknowledgment. The linear probe and linear spectral unmixing algorithm impose constraints on depth penetration and quantitative accuracy, necessitating expanded investigations. In vivo, unknown fluence distributions further complicate chromophore quantification, underscoring the need for future simulations to enable corrections. Relating PA and EMG observations remains challenging; for instance, the probe was positioned over the array but not necessarily the most active electrodes, potentially misaligning signals. Prospective refinements could include force signal recording to precisely delineate contraction endpoints (bypassing RMS maxima), probe relocation to EMG hotspots, and recruitment of additional subjects for robustness. In summary, this study establishes the feasibility of integrating PAI with HD-sEMG for non-invasive assessment of muscle hemodynamics and activation during fatigue. As a safe, radiation-free modality, PAI holds growing clinical promise, and its synergy with HD-sEMG could yield deeper insights into neuromuscular function, paving the way for enhanced diagnostic and rehabilitative applications.

Bibliography

[1] Na Li, Rui Zhou, Bharath Krishna, Ashirbad Pradhan, Hyowon Lee, Jiayuan He, and Ning Jiang. «Non-invasive techniques for muscle fatigue monitoring: A comprehensive survey». In: *ACM Computing Surveys* 56.9 (2024), pp. 1–40 (cit. on pp. 2, 15–18, 21).

[2] David G Allen, Graham Douglas Lamb, and H Westerblad. «Skeletal muscle fatigue: cellular mechanisms». In: *Physiological reviews* 88.1 (2008), pp. 287–332 (cit. on pp. 2, 6, 13, 15).

[3] Roger M Enoka and Jacques Duchateau. «Muscle fatigue: what, why and how it influences muscle function». In: *The Journal of physiology* 586.1 (2008), pp. 11–23 (cit. on p. 2).

[4] Hoda M Abd-Elfattah, Faten H Abdelazeim, and Shorouk Elshennawy. «Physical and cognitive consequences of fatigue: A review». In: *Journal of advanced research* 6.3 (2015), pp. 351–358 (cit. on p. 2).

[5] Wim Ament and Gijsbertus J Verkerke. «Exercise and fatigue». In: *Sports medicine* 39.5 (2009), pp. 389–422 (cit. on pp. 2, 21).

[6] Mohamed R Al-Mulla, Francisco Sepulveda, and Martin Colley. «A review of non-invasive techniques to detect and predict localised muscle fatigue». In: *Sensors* 11.4 (2011), pp. 3545–3594 (cit. on p. 3).

[7] Jing-jing Wan, Zhen Qin, Peng-yuan Wang, Yang Sun, and Xia Liu. «Muscle fatigue: general understanding and treatment». In: *Experimental & molecular medicine* 49.10 (2017), e384–e384 (cit. on pp. 3, 15, 16).

[8] Cindy L. Stanfield. *Fisiologia*. 5th ed. Italian edition. Napoli: EdiSES s.r.l., 2017 (cit. on pp. 4, 7).

[9] Carlo Gotti, Alberto Sensini, Andrea Zucchelli, Raffaella Carloni, and Maria Letizia Focarete. «Hierarchical fibrous structures for muscle-inspired soft-actuators: A review». In: *Applied Materials Today* 20 (2020), p. 100772 (cit. on p. 5).

[10] Paul B Gastin. «Energy system interaction and relative contribution during maximal exercise». In: *Sports medicine* 31.10 (2001), pp. 725–741 (cit. on p. 11).

[11] José Francisco Tornero-Aguilera, Jorge Jimenez-Morcillo, Alejandro Rubio-Zarapuz, and Vicente J Clemente-Suárez. «Central and peripheral fatigue in physical exercise explained: A narrative review». In: *International journal of environmental research and public health* 19.7 (2022), p. 3909 (cit. on p. 15).

[12] Amalina Binte Ebrahim Attia, Ghayathri Balasundaram, Mohesh Moothanchery, US Dinish, Renzhe Bi, Vasilis Ntziachristos, and Malini Olivo. «A review of clinical photoacoustic imaging: Current and future trends». In: *Photoacoustics* 16 (2019), p. 100144 (cit. on pp. 18–20).

[13] Dhiman Das, Arunima Sharma, Praveenbalaji Rajendran, and Manojit Pramanik. «Another decade of photoacoustic imaging». In: *Physics in Medicine & Biology* 66.5 (2021), 05TR01 (cit. on pp. 18, 19).

[14] Yinshi Yu, Ting Feng, Haixia Qiu, Ying Gu, Qian Chen, Chao Zuo, and Haigang Ma. «Simultaneous photoacoustic and ultrasound imaging: A review». In: *Ultrasonics* 139 (2024), p. 107277 (cit. on p. 18).

[15] Karl Kratkiewicz, Rayyan Manwar, Yang Zhou, Moein Mozaffarzadeh, and Kamran Avanaki. «Technical considerations in the Verasonics research ultrasound platform for developing a photoacoustic imaging system». In: *Biomedical Optics Express* 12.2 (2021), pp. 1050–1084 (cit. on pp. 18, 19, 25, 34).

[16] Hisham Assi et al. «A review of a strategic roadmapping exercise to advance clinical translation of photoacoustic imaging: from current barriers to future adoption». In: *Photoacoustics* 32 (2023), p. 100539 (cit. on p. 19).

[17] Jonas JM Riksen, Anton V Nikolaev, and Gijs van Soest. «Photoacoustic imaging on its way toward clinical utility: a tutorial review focusing on practical application in medicine». In: *Journal of biomedical optics* 28.12 (2023), pp. 121205–121205 (cit. on p. 19).

[18] Alexandra L Wagner et al. «Precision of handheld multispectral optoacoustic tomography for muscle imaging». In: *Photoacoustics* 21 (2021), p. 100220 (cit. on pp. 19, 53).

[19] Angelos Karlas et al. «Skeletal muscle optoacoustics reveals patterns of circulatory function and oxygen metabolism during exercise». In: *Photoacoustics* 30 (2023), p. 100468 (cit. on pp. 19, 53).

[20] Jinge Yang, Guang Zhang, Wu Chang, Zihui Chi, Qiquan Shang, Man Wu, Teng Pan, Lin Huang, and Huabei Jiang. «Photoacoustic imaging of hemodynamic changes in forearm skeletal muscle during cuff occlusion». In: *Biomedical optics express* 11.8 (2020), pp. 4560–4570 (cit. on pp. 19, 53).

[21] Angelos Karlas et al. «Multispectral optoacoustic tomography of peripheral arterial disease based on muscle hemoglobin gradients—a pilot clinical study». In: *Annals of translational medicine* 9.1 (2021), p. 36 (cit. on pp. 19, 20, 53).

[22] Anna P Träger et al. «Hybrid ultrasound and single wavelength optoacoustic imaging reveals muscle degeneration in peripheral artery disease». In: *Photoacoustics* 35 (2024), p. 100579 (cit. on pp. 19, 53).

[23] Adrian P Regensburger et al. «Multispectral optoacoustic tomography for non-invasive disease phenotyping in pediatric spinal muscular atrophy patients». In: *Photoacoustics* 25 (2022), p. 100315 (cit. on p. 19).

[24] Angelos Karlas et al. «Multispectral optoacoustic tomography of muscle perfusion and oxygenation under arterial and venous occlusion: A human pilot study». In: *Journal of biophotonics* 13.6 (2020), e201960169 (cit. on pp. 19, 53).

[25] Lina Tan et al. «Non-invasive optoacoustic imaging of glycogen-storage and muscle degeneration in late-onset Pompe disease». In: *Nature Communications* 15.1 (2024), p. 7843 (cit. on p. 19).

[26] Lu Ding, Xosé Luís Deán-Ben, Neal C Burton, Robert W Sobol, Vasilis Ntziachristos, and Daniel Razansky. «Constrained inversion and spectral unmixing in multispectral optoacoustic tomography». In: *IEEE transactions on medical imaging* 36.8 (2017), pp. 1676–1685 (cit. on p. 20).

[27] Stratis Tzoumas and Vasilis Ntziachristos. «Spectral unmixing techniques for optoacoustic imaging of tissue pathophysiology». In: *Philosophical Transactions of the Royal Society A: Mathematical, Physical and Engineering Sciences* 375.2107 (2017), p. 20170262 (cit. on pp. 20, 35).

[28] Gea Drost, Dick F Stegeman, Baziel GM van Engelen, and Machiel J Zwarts. «Clinical applications of high-density surface EMG: a systematic review». In: *Journal of Electromyography and Kinesiology* 16.6 (2006), pp. 586–602 (cit. on p. 21).

[29] Roberto Merletti, Marco Knaflitz, and Carlo J De Luca. «Myoelectric manifestations of fatigue in voluntary and electrically elicited contractions». In: *Journal of applied physiology* 69.5 (1990), pp. 1810–1820 (cit. on p. 21).

[30] Gazzoni Marco, Botter Alberto, and Vieira Taian. «Surface EMG and muscle fatigue: multi-channel approaches to the study of myoelectric manifestations of muscle fatigue». In: *Physiological measurement* 38.5 (2017), R27 (cit. on p. 21).

[31] Giacinto Luigi Cerone, Alberto Botter, and Marco Gazzoni. «A modular, smart, and wearable system for high density sEMG detection». In: *IEEE Transactions on Biomedical Engineering* 66.12 (2019), pp. 3371–3380 (cit. on p. 26).

[32] GL Cerone, A Giangrande, M Ghislieri, M Gazzoni, H Piitulainen, and A Botter. «Design and validation of a wireless body sensor network for integrated EEG and HD-sEMG acquisitions». In: *IEEE Transactions on Neural Systems and Rehabilitation Engineering* 30 (2022), pp. 61–71 (cit. on p. 26).

[33] Gael Diot, Stephan Metz, Aurelia Noske, Evangelos Liapis, Barbara Schroeder, Saak V Ovsepian, Reinhard Meier, Ernst Rummeny, and Vasilis Ntziachristos. «Multispectral optoacoustic tomography (MSOT) of human breast cancer». In: *Clinical Cancer Research* 23.22 (2017), pp. 6912–6922 (cit. on p. 31).

[34] Scott A. Prahl. *Optical absorption of hemoglobin*. Oregon Medical Laser Center. n.d. URL: `https://omlc.org/spectra/hemoglobin/` (visited on 08/25/2025) (cit. on p. 36).

[35] Vivek T Rathod. «A review of acoustic impedance matching techniques for piezoelectric sensors and transducers». In: *Sensors* 20.14 (2020), p. 4051 (cit. on p. 52).

[36] Rayyan Manwar, Loïc Saint-Martin, and Kamran Avanaki. «Couplants in acoustic biosensing systems». In: *Chemosensors* 10.5 (2022), p. 181 (cit. on p. 52).